Alexandria Engineering Journal 100 (2024) 153–169

Contents lists available at ScienceDirect

Alexandria Engineering Journal

journal homepage: www.elsevier.com/locate/aej

Review

A progression in the techniques of reducing RCS for the targets

Muhammad Ubaid Ullah [a], Tarik Bin Abdul Latef [a,*], Mohamadariff Othman [a], Mousa I. Hussein [b], Hamad M. Alkhoori [b], Yoshihide Yamada [c], Kamilia Kamardin [c], Raheela Khalid [d]

[a] Department of Electrical Engineering, Universiti Malaya, Kuala Lumpur, Malaysia
[b] Department of Electrical Engineering, United Arab Emirates University, Al Ain, United Arab Emirates
[c] Malaysia-Japan International Institute of Technology (MJIIT), Universiti Teknologi Malaysia, Kuala Lumpur 54100, Malaysia
[d] Department of Electrical Engineering, Bahauddin Zakariya University, Multan, Pakistan

ARTICLE INFO

Keywords:
RCS reduction
RCS reduction techniques
Scattering
Absorption
Stealth
Metasurface

ABSTRACT

This review is based on the radar cross-section (RCS) reduction techniques, with the prominence of the metasurface and its design. The thorough detail starts with introducing the concepts of the RCS and its reduction techniques. Then, traditional and recent techniques are provided to reduce RCS, emphasizing the scattering and absorption methods. An in-depth analysis of shaping processes and Radar Absorbing Materials (RAM) is provided, which are two standard RCS reduction techniques. It also thoroughly analyses the metamaterial-based RCS reduction, considering both active and passive configurations. The primary aspects covered regarding the utilization of metasurfaces for reducing RCS include profile, conformality, polarization sensitivity, and design complexity. To provide comparison and evaluation, the review includes tabulated information on performance parameters such as the method used, frequency range, size, optimization method, and planar or conformal design of RCS reduction. Additionally, the paper identifies areas within the field that require further in-depth research and investigation.

1. Introduction

RCS can be mathematically defined as 4π multiplied by the ratio of the power per unit solid angle dispersed in one direction to the power per unit solid angle of the incident plane wave from that direction [1]. Various factors contribute to the RCS, including the incidence angle, geometry, material properties, frequency, and polarization of the electromagnetic waves. RCS can be divided into two groups: monostatic and bistatic. The term monostatic RCS describes a situation in which the transmitter and receiver are in the same position, whereas the bistatic RCS occurs when the transmitter and receiver are positioned at different locations.

Reducing the range in which the radar can detect the target is the concept behind RCS reduction. In an ideal scenario, RCS reduction implies making the target completely undetectable by radar, regardless of the parameters and circumstances. However, in practical terms, 10 dB RCS reduction is referred to as adequate, corresponding to a 90% reduction in the detectability of the target [2].

RCS reduction has significant applications in both military and civil fields. One prominent area of focus is stealth technology, which has driven extensive research in RCS reduction. The roots of stealth technology can be traced back to World War I, when cellulose-based compounds were used to make weapons and aircraft less detectable. Similarly, during World War II, the Horten 229 V3 aircraft utilized a wooden covering to enhance its low observability and reduce detection [3]. In the realm of scientific advancements, a Russian scientist introduced a method for studying different electromagnetic wave scattering [4]. Furthermore, Lockheed Martin researchers developed the SR-71 stealth aircraft, which achieved RCS reduction using absorptive paint and an unconventional shape [5]. The RCS reduction in this plane is achieved with the help of absorptive paint, metamaterials, and unusual shapes.

The two primary methods of reducing RCS are scattering and absorption. The key distinction between these mechanisms lies in how they interact with radar signals. The radar signal is diverted away via a scattering mechanism, effectively reducing the radar cross-section, while absorption dissipates the signal by absorbing it in a specialized layer.

* Corresponding author.
E-mail address: tariqlatef@um.edu.my (T. Bin Abdul Latef).

https://doi.org/10.1016/j.aej.2024.05.001
Received 7 November 2023; Received in revised form 16 April 2024; Accepted 1 May 2024
Available online 21 May 2024
1110-0168/© 2024 The Author(s). Published by Elsevier BV on behalf of Faculty of Engineering, Alexandria University This is an open access article under the CC BY license (http://creativecommons.org/licenses/by/4.0/).

Using the shaping procedure, the incoming radar signal can be redirected away from the radar system in a scattering mechanism. On the other hand, RAM absorbs and dissipates the radar signal, preventing it from reflecting to the radar source. Both scattering and absorption techniques were used in the development of stealth technology. Because of the good qualities of metasurfaces, they have attracted much attention and popularity. A periodic or aperiodic array of subwavelength scatterers with electromagnetic properties is known as a metasurface [6]. Designing desired subwavelength scatterers makes it feasible to produce successful results, opening various applications. Numerous review papers have explored the applications of metasurfaces and metamaterials [7–12]. Metasurfaces, with their unique characteristics, are extensively used in RCS reduction, leveraging both scattering and absorption mechanisms.

This paper aims to provide a comprehensive review of various techniques for reducing RCS, with a specific focus on the scattering and absorption mechanisms. The discussion will encompass both traditional and contemporary methods, offering insights into the limitations of each approach. Importantly, this review will delve into the mechanisms employed for RCS reduction and the techniques utilized for constructing metasurfaces, offering a novel and comprehensive perspective. By synthesizing existing literature and conducting a comparative analysis, this paper fills a gap in the current understanding of RCS reduction. It serves as a valuable resource for researchers seeking to stay informed about recent advancements and provides essential insights into the complex techniques of RCS reduction.

2. Application of RCS reduction

Radar technology is being extensively used in various applications, such as in aircraft and ships, detection of insects [13], speed measurement [14], etc. RCS is referred to as the measurement of electromagnetic nature using radars. There exist some scenarios when the object needs not to be detected or has low detectability, as mentioned below:

- Military stealth aircraft and ships need low detectability to prevent them from being attacked by opposition.
- RCS reduction without mitigating the effect of radiating characteristics of an antenna [15]. The antennas increase the RCS, increasing the visibility of aircraft and ships, which is a sign of danger, so RCS should be decreased.
- Parking decks of aircraft need to have low RCS as well because it is typically near airports; the reflection from the deck interferes with the airport's navigation system. Therefore, RCS reduction is essential [16].

3. RCS reduction techniques

Fig. 1 illustrates the various techniques employed for RCS reduction. Two primary techniques of utmost importance in RCS reduction are scattering and absorption. Scattering can be further subdivided into two techniques: shaping and metasurface. Shaping is a conventional method widely used in RCS reduction, while using metasurfaces is gaining prominence in modern research. Similarly, in the case of absorption, the conventional technique employed is RAM, which is applied over the target to reduce RCS. Metasurfaces are utilized in both scattering and absorption methods for RCS reduction. In this review, the primary focus is on metasurfaces while also discussing shaping and RAM techniques.

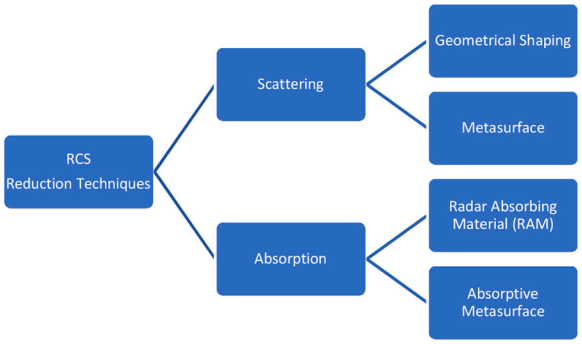


Fig. 1. Radar cross section reduction techniques.

3.1. Geometrical shaping

The geometrical shaping technique has proven to be highly beneficial in monostatic radars [17]; it is referred to as a method to modify the shape of an object to reduce the RCS. Two primary approaches are employed in shaping to reduce RCS, aimed at minimizing reflections back to the radar, (i) a compact, smooth, and blended exterior geometry must be imposed, and (ii) a faceted design must be used.

In 1981, an unmanned aircraft was developed with a diamond-shaped cross-section and a flat lower surface to reduce glint which significantly reducing detectability [18]. The implementation of a smooth curved shape has been successful in achieving low RCS.

Optimizing the shape of the target itself to reduce RCS is discussed in [19] and [20], where the shape is modified to meet specific requirements. However, shaping techniques do have certain limitations. They only apply to specific incident wave angles and over a limited bandwidth [21]. To mitigate the bandwidth limitation, gradient shapes can be used. Nevertheless, shaping techniques may not be suitable for large targets such as planes and ships, as they can potentially affect the internal volume and stability of the target [21].

3.2. Radar absorbing material (RAM)

RAM is the method used for the reduction of RCS; it is categorized in two on its functionality [22]:

i. Impedance matching.
ii. Resonance.

3.2.1. Impedance matched RAM

RAM comes in three different shapes: pyramidal, tapered, and matching. Fig. 2(a) illustrates a pyramidal absorber for a semi-anechoic chamber reported in [23]. A tapered RAM consists of a low-loss material slab having lossy material homology spread parallel to the surface. This type of material converts the energy incident into the heat. The Lockheed F-117 Nighthawk aircraft employed a tapered RAM of carbonyl iron balls dispersed in epoxy resin to reduce RCS [24]. A matching layer absorber is present between the incident absorbing point, which provides absorption properties to the model [25], as shown in Fig. 2(b). If adequate matching is necessary, the matching layer thickness must be one-quarter the wavelength of the radiation of the layer; this configuration helps to convert it to narrowband absorbers.

3.2.2. Resonant RAM

Another name for resonant RAM is tuned or quarter wavelength absorber. This method results in an impedance mismatch between the incident and the absorbing material. The reflection of the wave first gets a phase shift of π. While traveling through an absorbing medium, the metal back element reflects the electromagnetic wave being sent. For this reason, the second reversal produces the reversal of π, before backwave propagate into the incident medium. That would result in a destructive interference between two waves that is reflected, reducing RCS. Salisbury screen [26] and Jaumann absorber [27] are used as a resonant RAM. RAM provides a narrow bandwidth and is usually thick, but the bandwidth enhancement can be done by increasing the thickness of the model. Still, it results in low usage for practical applications.

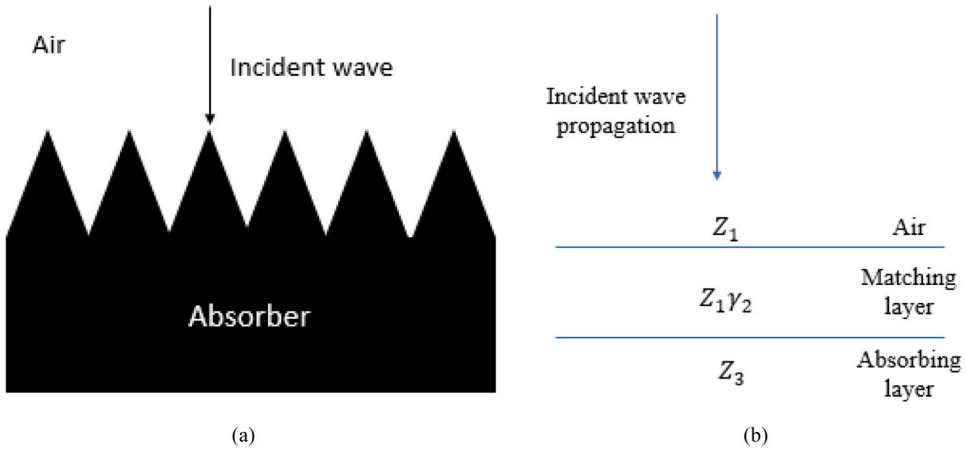


Fig. 2. Representation of (a) Pyramid absorber and (b) matched layer absorption [22].

3.3. RCS reduction on scattering mechanisms

Metasurfaces are made to manipulate the reflection amplitudes and phases of incident waves. The arrangement of cells in various patterns gives rise to macrocells and tiles, forming metasurfaces. The behavior of a metasurface is determined by the positioning and geometric configuration of elements within its unit cells. Based on their functionalities, metasurfaces can be categorized as follows:

I. Phase gradient metasurface (PGMS).
II. Checkboard Metasurface (CMS).
III. Polarization conversion metasurface (PCMS).
IV. Coding-based metasurface (COM).
V. Reconfigurable metasurface (RMS).
VI. Time-varying metasurface (TVM).

For lowering RCS, the first four are passive approaches, and the final two are active.

The Huygens metasurface and bi-anisotropic metasurfaces can be used to describe the phenomenon of wavefront manipulation. According to [28–30], the Huygens surface creates impedance and admittance to reflect or refract the incident wave at various angles. This design can aid in reducing the RCS for practical applications. In [31], the synthesis technique makes omega-bi-anisotropic metasurface (O-BMSs). The surface reflects the incident wave in an appropriate direction for RCS reduction. Huygens and bi-anisotropic metasurface can be employed as polarization conversion metasurfaces [32,33].

3.3.1. Phase gradient metasurface

The propagating wave conversion and anomalous reflection are being carried out in the PGMS for the RCS reduction. The concept of PGMS is related to diffraction gratings. It became famous after the Snell's law advancement [34]. Snell's Law implies that phase discontinuities that divert the signal away from its intended direction of propagation, as given in the expression:

$$sin(\theta_t)n_t - sin(\theta_i)n_i = (\lambda_o/2\pi)(d\varphi/dx) \quad (1)$$

The n_t and n_i refractive indices of two different media; $d\varphi$ is the phase difference between the cells; dx is spacing between the elements, whereas λ_o is known as the free space wavelength. In the PGMS, the elements designed should have the span of 2π phase range as presented in the expression 1.

PGMS can be practically explained using V-shaped nano-antennas [34]. The components of PGMS can alter the wave's reflection phase and amplitude. The components are placed in a gradient pattern, which is then replicated to create the phase gradient metasurface. The main challenge lies in achieving broadband elements, as the unit cell size must be carefully considered relative to the operating frequency range.

The specular reflection of the graded index structure can be decreased in two ways:

- Anomalous reflection [35].
- Propagating wave to surface wave conversion [36].

A mismatch in polarization plays a significant role in achieving low detectability by other radars. Modifying symmetric resonators is necessary for polarization-insensitive phase gradient metasurfaces to change the phase of reflected and transmitted waves. However, the bandwidth of symmetric resonators is limited. To broaden the bandwidth for anomalous reflection and polarization conversion, several methods have been proposed, including combining multiple resonators [37]. The waves can be divided into equal-amplitude left-handed circular polarization (LCP) and right-handed circular polarization (RCP) based on the polarization theory of linearly polarized (LP) waves. In [38], a reflective phase gradient metasurface for circularly polarized (CP) waves is used to generate a wideband polarization-insensitive anomalous reflection of LP waves. Additionally, a metasurface with N-shaped metallic resonators is proposed to maintain efficient wideband polarization reflection for both LCP and RCP incidences.

In [39], a phase gradient metasurface coupled to an absorptive frequency-selective surface made of metallic square loops and lumped resistors. This method reduces the RCS by about 13 dB for the frequency range of 5.6–16 GHz and a bandwidth of 10.4 GHz as shown in Fig. 3.

Low-Quality (Q) metasurfaces presented in [40] have shown a significant 40% reduction in radar RCS. Additionally, researchers have developed a variety of elements with wideband characteristics using a gradient approach. In [41], an ultra-thin hybrid technology based on Phase Gradient Metasurfaces (PGMS) demonstrated RCS reduction in the 8.7 GHz and 11.4 GHz frequency bands. Circularly polarized waves are used to reduce wideband RCS using PGMS with the Pancharatnam-Berry phase, as presented in [42]. By employing both surface wave conversion and anomalous reflection, split ring-based PGMS has achieved an increased bandwidth of up to 74% for RCS reduction [43]. The paper addresses the cost-effectiveness aspect by proposing a metasurface model that provides a broader bandwidth of 128% and a reflection amplitude and phase angle of 60°, as referenced in [44]. In [45], a novel approach combining an artificial magnetic conductor (AMC) and a phase gradient frequency-selective metasurface was proposed for a Fabry-Perot cavity antenna; this design achieved an RCS reduction of approximately 12.36 dB within the frequency range of 4–13 GHz as presented in Fig. 4.

The mentioned works primarily focus on flat metal targets, but it is important to consider oblique incidences for both flat and conformal surfaces in the RCS reduction of antennas. The work in [46], a

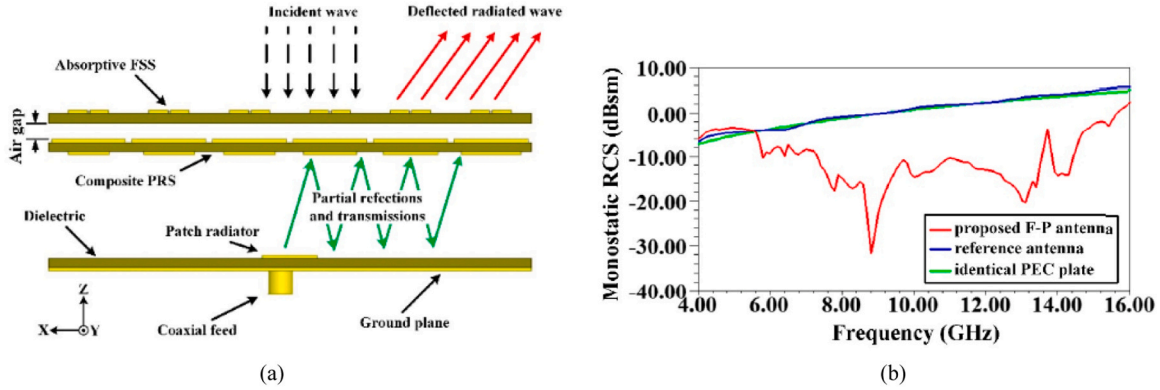


Fig. 3. (a) Designed antenna schematics, (b) Monostatic RCS of x-polarized wave [39].

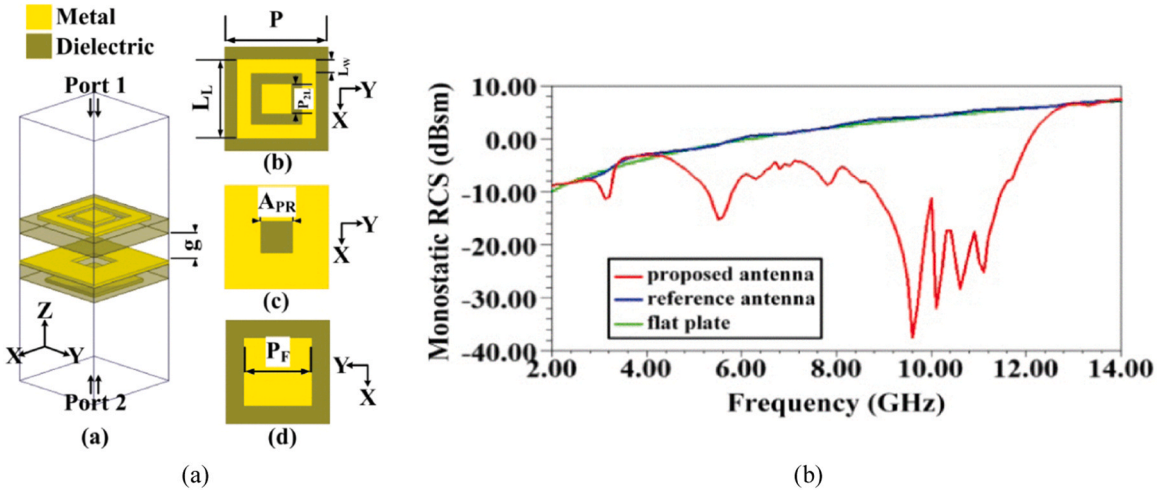


Fig. 4. (a) Proposed antenna design and (b) monostatic RCS reduction of VP antenna [45].

windmill-shaped element was used under oblique incidences, resulting in a wide output angle of 25° and effective RCS reduction. For slot array antenna RCS reduction, PGMS was employed in [47], operating in the frequency range of 4.1–4.26 GHz; notably, RCS reduction was achieved in the out-of-band frequency range of 7–16.8 GHz. These findings highlight the significance of considering oblique incidences and employing various metasurface designs to effectively reduce RCS in antennas and other applications specially in conformal designs.

The factors that will improve the bandwidth of the PGMS are:

I. The selection of the right element having a phase range of 2π of the wideband.
II. The design of an element that coincides with both PW to SW conversion and anomalous reflection.

The PGMS published work is summarized in Table 1:

3.3.2. *Checkerboard metasurface*

This metasurface is made up of two subarrays that are arranged in a checkerboard-like pattern and operate on the principle of destructive interference. Within this structure, the unit cells are organized irregularly. Two adjacent unit cells are intended to reflect waves at angles of 0° and 180°, respectively. As a result, the reflected signals cancel each other out in the far field.

The checkerboard metasurface for reducing RCS was first introduced in [48], illustrated in Fig. 5(a). The study presents a checkerboard structure comprising a perfect electric conductor (PEC) and an AMC. Through the collaborative action of AMC and PEC, which induce reflection phases of 0° and 180° respectively, destructive interference in the far field results, leading to a reduction in RCS. Nonetheless, this configuration is constrained by its limited effective bandwidth. In [49], the idea of using an AMC-AMC pair instead of an AMC-PEC pair is proposed as shown in Fig. 5(b), demonstrating that this arrangement provides a wider bandwidth compared to the AMC-PEC pair. Researchers have also investigated suitable combinations of metasurface components to increase bandwidth.

The work in [50] describes achieving a bandwidth of 32% by adjusting the phase difference between two artificial magnetic conductors (AMCs) to be within ±30°, resulting in reduced RCS. In [51], the utilization of a Jerusalem cross-based checkerboard arrangement is discussed, highlighting the direction of grating lobes and offering a bandwidth of 40%. The [52] provides a formula for RCS reduction based on the reflection coefficient and phase of unit cells, emphasizing the necessity of a phase variation of 180° ± 38° between unit cells to achieve a 10 dB reduction in RCS.

$$RCS_{reduction} = \left| \frac{A_1 e^{j\varphi_1} + A_2 e^{j\varphi_2}}{2} \right| \quad (2)$$

The A1 and A2 represent the amplitude, whereas φ_1 and φ_2 represent the phases of unit cells 1,2, respectively.

In [53], a dual resonance unit cell is introduced to reduce dual-band RCS, effectively lowering RCS within two frequency bands. In [54], the authors present a single and dual resonance artificial magnetic conductor (AMC) with an 83% bandwidth. Additionally, they use four

Table 1
Phase gradient metasurface Comparison.

Sr. No	Ref. No	Working Mechanism	a) RCS reduction frequency range b) Monostatic/Bistatic		Unit cell size	Array size	Conformal Design
			Simulated Result	Measured Result			
1	[36]	Propagating to Surface wave conversion	15 GHZ Monostatic	15 GHZ Monostatic	0.125λo x 0.3λo	-	No
2	[37]	Anomalous reflection	9–19 GHz Monostatic	9–19 GHz Monostatic	0.18λo x 0.18λo	12λo x 12λo	No
3	[38]	Anomalous reflection	9.2–17.7 GHz Monostatic	9.2–17.7 GHz Monostatic	0.16λo x 0.16λo	11.7λo x 11.7λo	No
4	[39]	Absorptive FSS + Propagating to Surface wave conversion	5.6–16 GHz Monostatic	5.6–16 GHz Monostatic	0.16λo x 0.16λo	2.11λo x 2.11λo	No
5	[40]	Anomalous reflection	8–11 GHz Monostatic	8–11 GHz Monostatic	0.16λo x 0.23λo	-	No
6	[41]	Anomalous reflection	8.9–11.4 GHz Monostatic	8.9–11.4 GHz Monostatic	0.20λo x 0.20λo	10.4λo x 10.4λo	No
7	[42]	Anomalous reflection	9.85–19.37 GHz Monostatic	9.85–19.37 GHz Monostatic	0.25λo x 0.25λo	8.25λo x 8.25λo	No
8	[43]	Propagating to Surface wave conversion + Anomalous reflection	8–13 GHZ Monostatic	8–13 GHZ Monostatic	0.40λo x 0.40λo	8.10λo x 8.10λo	No
9	[44]	Anomalous reflection	9–40.7 GHz Monostatic	9–40.7 GHz Monostatic/ Bistatic	0.75λo x 0.75λo	19λo x 19λo	No
10	[45]	Anomalous reflection	Ant-1: 4–13 GHz Monostatic Ant-2: 4–13 (VP) 5.2–13 (HP) Monostatic	Ant-1: 4–13 GHz Monostatic Ant-2: 4–13 (VP) 5.2–13 (HP) Monostatic	Ant-1 and Ant-2: 0.17λo x 0.17λo	Ant-1: 1.56λo x 1.56λo and Ant-2: 1.38λo x 1.04λo	No
11	[46]	Anomalous reflection	8–13 GHz Monostatic	8–13 GHz Monostatic	0.20λo x 0.20λo	10.5λo x 10.5λo	No
12	[47]	Anomalous reflection	7–16.8 GHz Monostatic	7–16.8 GHz Monostatic	0.42λo x 0.42λo	1.71λo x 1.71λo	No

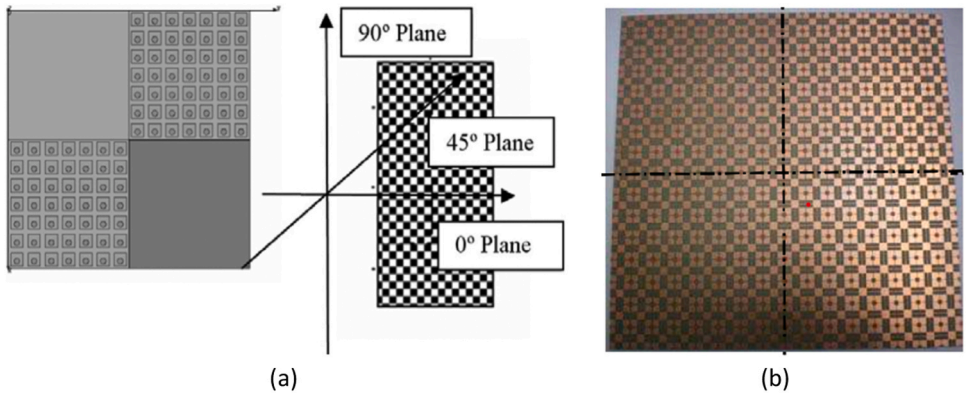


Fig. 5. Proposed unit cell arrangement design of (a) AMC-PEC chessboard metasurface [48] and AMC metasurface [49].

AMCs with a 180° ± 37° phase variation to increase bandwidth by up to 91%. The combination of dual and triple AMCs is employed in [55] to achieve a bandwidth of 91.5%. The authors analytically provide the checkerboard configuration using an equivalent transmission line model. By utilizing arcs at the corners and implementing surface wave suppression techniques, a bandwidth improvement of 60–65% is achieved [56]. In [57], a combination of an AMC and a partially reflecting surface (PRS) is proposed using a meander line checkerboard metasurface configuration to achieve RCS reduction.

In [58], a broader bandwidth ratio (*fH/fL*) of 5.87:1 under normal incidence is achieved by employing a multi-element non-planar checkerboard metasurface. The reduction in RCS is accomplished through the scattered cancellation of several elements. In [59], a triple-layered checkerboard structure is introduced that offers an impressive 96% bandwidth for RCS reduction. In [60], a comprehensive explanation of the checkerboard configuration and phase gradient is provided. The paper not only presents synthesis processes utilizing Schelkunoff's polynomial approach and the phasor diagram method but also delves into concepts such as Snell's law and array theory.

The work of [61] uses the improved fruitfly optimization mechanism to get the unit cell dimensions and increase the bandwidth of broadband structures. This approach leads to an additional RCS reduction of approximately 15 dB, with a bandwidth of 48%. While most of the works employ Rogers substrate, [62] proposes the use of a low-cost FR4 substrate with a phase deviation criterion for achieving wide bandwidth in CMS designs.

It should be noted that the previously mentioned checkerboard metasurfaces were primarily utilized for RCS reduction of flat metal targets. However, there is also a growing demand for RCS reduction of conformed surface metal targets. In [63], a solution for RCS reduction of conformed surface metal targets is proposed, specifically focusing on dihedral corners. This work addresses the challenges associated with curved surfaces and offers a method for RCS reduction in such scenarios. Additionally, [64] presents a low-cost, small-thickness hybrid checkerboard metasurface designed for wideband RCS reduction. This approach aims to address the practical considerations of cost and size while

achieving effective RCS reduction.

In [65] and [66], different approaches are proposed for reducing RCS of curved targets. [65] addresses the RCS reduction problem for curved targets using the AMC theory, while [66] tackles it through the ray tracing theory.

The bandwidth can be increased by the help of two factors:

i) With an appropriate choice of elements
ii) Surface wave suppression.

A summary of the proposed work is summarized in the given Table 2:

3.3.3. Polarization conversion metasurface

This metasurface achieves RCS reduction through polarization conversion. The design of its elements plays a crucial role in constructing the PCMS, as it transforms the polarization wave into an orthogonal state during reflection. This transformation reduces RCS since the radar cannot detect the reflected signal. The effectiveness of the metasurface is determined by its polarization conversion efficiency. The work presented in [67] is referenced as an example of polarization conversion metasurfaces, as seen in Figs. 6(a) and 6(b).

Along with the v- and u-axes, the electric field component produces both symmetric and asymmetric fields, respectively. When a polarized wave deploys in the x-direction, the electric field Ei separates into Eiv and Eiu components. Erv and Eiv are reflections that are out of phase because the function in the v-direction is of Perfect Electric Conductor (PEC) due to electric resonance. As a result of its increased impedance, the function in the u-direction is seen as a high-impedance surface and creates the in-phase reflections Eru and Eiu.

The remaining reflected wave consists of Erv and Eru, the Y-polarized components obtained by modifying the incident x-polarized wave Ei. The behavior of Element 1 in Fig. 7 is opposite to this. The reflected wave now includes x-co and cross-polarized components, Rxy and Ryy, as concluded from the expression provided in [67].

$$R_{xy} = \frac{|E_{rx}|}{|E_{iy}|} = \sqrt{\frac{(1-\cos\Delta\varphi)}{2}}$$

$$R_{yy} = \frac{|E_{ry}|}{|E_{iy}|} = \sqrt{\frac{(1+\cos\Delta\varphi)}{2}}$$

The $\Delta\varphi$ represents the phase difference between Rxy and Ryy, while the polarization conversion ration can be termed as [67]:

$$PCR = \frac{R^2{}_{xy}}{R^2{}_{xy} + R^2{}_{yy}} \tag{3}$$

In [68], a polarization conversion metasurface featuring an arrow element with double heads is presented; this metasurface in four frequencies achieves full polarization conversion, giving a 10 dB reduction in RCS in the 6.6–23.9 GHz frequency range. In [69], a new oblique split ring wire resonator is introduced over the frequency range of 9.4–19.2 GHz, offering a 10 dB RCS reduction. The Polarization Reflection Reflective Surface (PRRS) described in [70] is made up of a periodic array of quasi-L-shaped patches, and it has a PCR of more than 50% and a bandwidth of 103%.

In the frequency range of 17–42 GHz, [71] presents a method involving adding rotated unit cells to a checkerboard metasurface, resulting in a 10 dB RCS reduction across. This configuration enables wideband operation with angles up to 50°. The elements described in [72] consist of the dielectric substrate with square metallic patches placed above a ground plane; the superstrate encompasses a dual-patch unit cell, achieving an approximate 98% reduction in RCS at a 10 dB threshold. A polarization conversion metasurface is introduced in [73]; this metasurface achieves a 10 dB RCS reduction in the frequency range of 9–40 GHz, which refers to an approximately 126.5% reduction for TM and TE-polarized waves. It uses two-headed arrow cells with rotations of 90°, 180°, and 270° to create destructive interference.

In [74–77], appropriate elements allow for enhanced bandwidth, as

Table 2
Checkerboard metasurface Comparison.

Sr.No	Ref. No	a) RCS reduction frequency range b) Monostatic/Bistatic		Unit cell size	Array Size	Conformal Design
		Simulated Result	Measured Result			
1	[48]	15.32 GHz Monostatic/Bistatic	15.32 GHz Monostatic/Bistatic	1λo x 1λo	22λo x 14λo	No
2	[61]	4.8–14.8 GHz Monostatic/Bistatic	4.89–14.3 GHz Monostatic	0.49λo x 0.49λo	7.8λo x 7.8λo	No
3	[49]	5.78 GHz Monostatic	5.78 GHz Monostatic	0.18λo x 0.18λo	3.5λo x 3.5λo	No
4	[51]	14.4–28.8 GHz Monostatic/Bistatic	14.8–22.7 GHz Monostatic/Bistatic	0.25λo x 0.25λo	20.7λo x 13.8λo	No
5	[52]	4.10–7.59 GHz Monostatic/Bistatic	3.8–8.8 GHz Monostatic	0.29λo x 0.29λo	4.68λo x 4.68λo	No
6	[53]	3.94–7.40 GHz and 8.41–10.72 GHz Monostatic	3.94–7.40 GHz and 8.41–10.72 GHz Monostatic	0.34λo x 0.34λo	2.1λo x 2.1λo	No
7	[54]	3.75–10 GHz Monostatic/Bistatic	3.75–10 GHz Monostatic/Bistatic	0.32λo x 0.32λo	2.6λo x 2.6λo	No
8	[55]	3.78–10.08 GHz Monostatic/Bistatic	3.77–10.14 GHz Monostatic/Bistatic	0.37λo x 0.37λo	2.98λo x 2.98λo	No
9	[56]	8–16 GHz Monostatic/Bistatic	7.98–16.32 GHz Monostatic	0.6λo x 0.6λo	6λo x 6λo	No
10	[57]	4.5–6.5 GHz Monostatic	4.5–6.5 GHz Monostatic	0.4λo x 0.4λo	1.3λo x 1.3λo	No
11	[58]	5.5–32.3 GHz Monostatic/Bistatic	5.5–32.3 GHz Monostatic	0.5λo x 0.5λo	14λo x 14λo	No
12	[62]	4.3–12.6 GHz Monostatic	4.1–12.3 GHz Monostatic	0.41λo x 0.41λo	6.56λo x 6.56λo	No
13	[64]	15.8–19.3 and 21.4–36.5 GHz Monostatic/Bistatic	15.8–19.3 and 21.4–36.5 GHz Monostatic/Bistatic	0.22λo x 0.22λo	13.33λo x 13.33λo	No
14	[65]	7.2–8.6 GHz Monostatic	7.2–8.6 GHz Monostatic	0.25λo x 0.25λo	5λo x 5λo	Yes
15	[66]	12–24 GHz Monostatic	12–24 GHz Monostatic	0.2λo x 0.2λo	0.6λo x 0.6λo	Yes

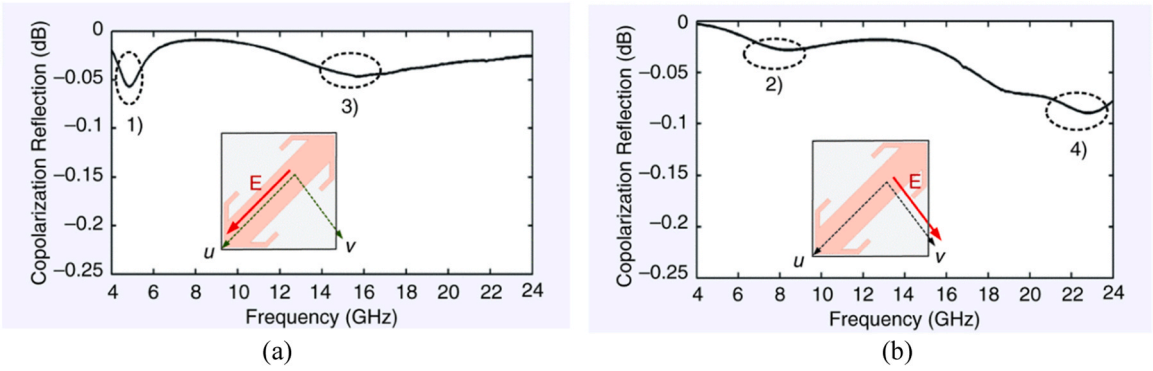


Fig. 6. Four resonances of the unit cell in normal incidence: (a) U polarized case, and (b) V polarized case [67].

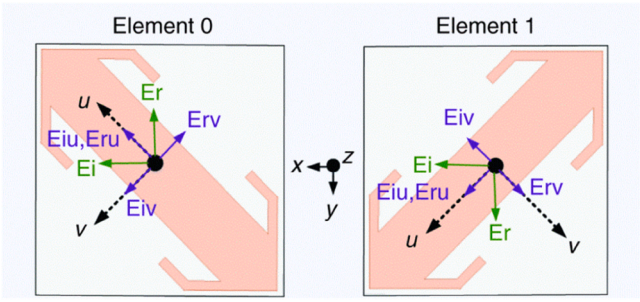


Fig. 7. An intuitive image of the x-polarized wave incident in the unit cell element 0 and unit cell element 1 [67].

demonstrated through the representation of diagonally arrow structures in the unit cells. Until now, the presented models have focused on RCS reduction of flat metal targets. However, further discussions on RCS reduction related to PCMS for oblique incidences are provided.

The [78–83] present the RCS reduction technique using PCMS. In [78], the paper discusses the combination of PRS with PCMS, aiming to enhance antenna gain while simultaneously reducing antenna RCS. The proposed design involves introducing a Fabry-Perot resonant cavity utilizing PCMS and PRS printed on two sides of the substrate above a microstrip patch antenna. By symmetrically arranging PCMS units and their mirror images, a significant reduction in RCS is achieved. The maximum reduction within the in-band frequency at 9.4 GHz reaches 20 dB, while the reported out-of-band reduction is 33 dB. The [79] reports a functional bandwidth of approximately 99.5% over a wideband on x and y-polarized waves, with a PCR of about 96%.

Metamaterials offer advantages such as low profile, flexible design, and high performance. They consist of two-dimensional materials containing subwavelength structures arranged in periodic or disordered patterns. In [84], a quaternionic meta surface with two pairs of unit cells is presented for bandwidth enhancement for reducing RCS. The overlapping bandwidth of the two units facilitates broadband and robust RCS reduction. The primary construction comprises square plates and square rings with a pitch of 6 mm and a depth of 2.035 mm. By incorporating cut-wire elements oriented at 45° and 135°, the metasurface achieves the necessary 180° phase difference across a wide frequency range for the checkerboard arrangement aimed at RCS reduction. The combined effect of the two pairs of unit cells results in an effective phase difference of 180° ± 60°, contributing to RCS reduction within the 13–33 GHz frequency range, as depicted in Fig. 8.

In [85], complementary units are introduced for estimating orthogonal-to-linear and linear-to-circular polarization conversions in a planar design. Conversely, [86] presents a polarization conversion design for both planar and conformal (up to 60°) configurations, achieving a 10 dB reduction in RCS within the Ultra-Wideband (UWB) frequency range of 6.3–20.5 GHz.

To sum up the overall PCMS discussion, a comparison of the different models and their parameters is presented below in Table 3:

3.3.4. *Coding metasurface*

The coding metasurface introduces a novel design approach that modifies the propagation of electromagnetic (EM) waves. It employs different phase element meta-atoms arranged on the metasurface, utilizing coding sequences to achieve specific functionalities. The one-bit coding metasurface, for instance, illustrates RCS reduction by

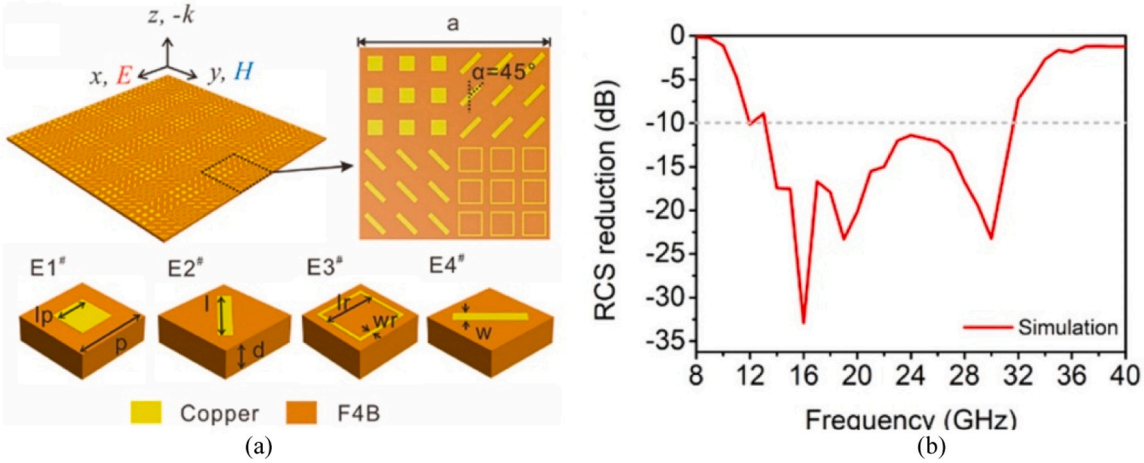


Fig. 8. The schematic structure of the (a) proposed design and (b) RCS reduction result [84].

Table 3
Polarization Conversion Metasurface Comparison.

Sr. No	Ref. No	Method Used	a) RCS reduction frequency range b) Monostatic/Bistatic		Unit cell size	Array Size	Conformal Design
			Simulated Result	Measured Result			
1	[68]	Polarization conversion through multiple plasmon resonance	6.8, 15.45, 12.17 and 23.13 GHz Monostatic	6.8, 15.45, 12.17 and 23.13 GHz Monostatic	0.3λo x 0.3λo	20λo x 20λo	No
2	[69]	Polarization Conversion	10.2–19.3 GHz Monostatic	10.2–19.3 GHz Monostatic	0.29λo x 0.29λo	3.4λo x 3.4λo	No
3	[70]	Polarization rotation reflective surface	10.74–17.2 GHz Monostatic	10.74–17.2 GHz Monostatic	0.28λo x 0.28λo	22λo x 14λo	No
4	[71]	Polarization Conversion + Coding Metasurface	17–42 GHz Monostatic/Bistatic	17–42 GHz Monostatic	0.30λo x 0.30λo	21λo x 21λo	No
5	[73]	Polarization Conversion	14.5–41 GHz Monostatic/Bistatic	16.8–37.3 GHz Monostatic/Bistatic	0.59λo x 0.59λo	16λo x 16λo	No
6	[74]	Polarization Conversion + Coding Metasurface	6–14 GHz Monostatic/Bistatic	6–14 GHz Monostatic/Bistatic	0.2λo x 0.2λo	8λo x 8λo	No
7	[75]	Random phase encoding polarization conversion	8.2–25.6 GHz Monostatic/Bistatic	8.2–25.6 GHz Monostatic/Bistatic	0.16λo x 0.16λo	4λo x 4λo	No
8	[76]	Linear wave to orthogonal wave polarization conversion	16.8–37.3 GHz Monostatic	16.8–27.3 GHz Monostatic	0.37λo x 0.37λo	15.05λo x 15.05λo	No
9	[78]	Polarization conversion + Partial reflection	9–20 GHz Monostatic	9–20 GHz Monostatic	0.19λo x 0.19λo	1.18λo x 1.18λo	No
10	[79]	Polarization Conversion	4.5–13 GHz Monostatic/Bistatic	4.5–13 GHz Monostatic/Bistatic	0.20λo x 0.20λo	1.67λo x 1.67λo	No
11	[80]	Polarization conversion	17.5–31.7 GHz Monostatic/Bistatic	17.5–31.7 GHz Monostatic/Bistatic	0.38λo x 0.38λo	4.58λo x 4.58λo	No
12	[82]	Polarization conversion + Coding metasurface	1.9–5.5 THz Monostatic	1.9–5.5 THz Monostatic	0.22λo x 0.22λo	3.64λo x 3.64λo	No
13	[83]	Polarization conversion + coding metasurface	9.5–13.9 and 15.2–20.4 GHz Monostatic/Bistatic	10.2–14.0 and 15.3–20.7 GHz Monostatic/Bistatic	0.5λo x 0.5λo	12λo x 12λo	No
14	[84]	Destructive phase difference with polarization conversion	13–33 GHz Bistatic	13–33 GHz Bistatic	0.26λo x 0.26λo	7.82λo x 7.82λo	No
15	[85]	Orthogonal linear and linear-to-circular polarization conversion	8.9–9.7 GHz and 15.5–26.1 GHz Monostatic	8.9–9.7 GHz and 15.5–26.1 GHz Monostatic	0.45λo x 0.45λo	-	No
16	[86]	Polarization conversion with different unit cell	5.5–20.5 GHz Monostatic/Bistatic	5.5–20.5 GHz Monostatic/Bistatic	0.14λo x 0.14λo	3.27λo x 3.27λo	Yes

integrating two meta-atoms that result in reflected wave fronts that are 180° out of phase. By optimizing patterns on the surface using algorithms and manipulating ones and zeros, the scattered wave can be controlled and tailored. The concept of binary digit metasurface unit cells as digital metamaterials was initially introduced in [87]. Multiple functionalities of metasurfaces with RCS reduction are discussed in [88]. In [89], a 2-bit coding metasurface that operates between 8.0 and 22.76 GHz. It is made up of four digital components that are based on a pattern of metallic double-cross lines.

By using unit cells in the metasurface that correspond to the digits 0 and 1, respectively, the binary coding metasurface achieves phase responses of 0° and 180°. Like this, the 4-element 2-bit coding metasurfaces have phases of 0°, 90°, 180°, and 270°. The equation below can be used to calculate the directivity and far-field pattern of a coding metasurface for RCS reduction:

$$f(\theta,\varphi) = f_e(\theta\varphi)\sum_{m=1}^{N} \times \sum_{n=1}^{N}\exp\left[-i\left\{\varphi(m,n)+kD\sin\theta\left[\left(m-\frac{1}{2}\right)\cos\varphi+\left(n-\frac{1}{2}\right)\sin\varphi\right]\right\}\right] \quad (4)$$

$$RCS_{reduction} = \frac{\lambda^2}{4\pi N^2 D^2}[Dir(\theta,\varphi)] \quad (5)$$

The elevation and azimuthal angles are represented by θ and φ, respectively. The spacing between the elements is denoted as D, while k represents the wavenumber. N is for the total number of items in the array, and φ(m,n) represents the phase of reflection of each element at the (m,n) position.

A checkerboard metasurface is considered a 1-bit coding metasurface, whereas the phase gradient metasurface is regarded as a multi-bit coded metasurface. [90–92] discusses the reflection and scattering of THz waves utilizing coding metasurfaces. In [90], a one-bit coding approach based on metallic ring resonators is presented. However, [91] introduces 1-bit, 2-bit, and multi-bit coding using Minkowski closed-loop elements. A unit element design for optimized coding metasurfaces with low Q-factor is proposed in [93], employing the genetic algorithm and nonlinear fitting method for RCS reduction. Additionally, [94] more than 10 dB RCS reduction presented by a small-sized coding metasurface, combining particle swarm optimization with far-field scattering characteristics for coding sequence optimization.

The coding phase gradient is discussed in [42], where N-shaped elements are used as unit cells with co-polarized reflected characteristics for incident waves. The Pancharatnam-Berry phase is used in 1-bit, 2-bit, and multi-bit coding designs. Based on the angle of incidence, the equations below define the direction of the reflected wave:

$$\theta_b = \sin^{-1}\left(\frac{\sqrt{(k_0\sin\theta_i\cos\varphi_i+\nabla\varphi_i)^2+(k_0\sin\theta_i\cos\varphi_i+\nabla\varphi_y)^2}}{k_0}\right) \quad (6)$$

$$\varphi_b = \tan^{-1}\left(\frac{k_0\sin\theta_i\cos\varphi_i+\nabla\varphi_y}{k_0\sin\theta_i\cos\varphi_i+\nabla\varphi_x}\right) \quad (7)$$

The θ_b and φ_b represent the azimuth angle of the main lobe whereas $\nabla\varphi_x = \frac{d\varphi_x}{dx}$, $\nabla\varphi_x = \frac{d\varphi_y}{dx}$ represents the phase gradient in x and y-direction. The unit cells' length and breadth are expressed as dx and dy. The phase

difference is given as $d\varphi_x$ and $d\varphi_y$ respectively.

In [67,96–98], an optimized design approach for bandwidth enhancement of coded metasurfaces is presented. According to [96], combining coding metasurfaces and bandpass frequency selective surface techniques achieves high-efficiency transmission and broadband RCS reduction. For 1-bit and 2-bit coding metasurfaces, theoretical and experimental demonstrations operating at THz frequencies are presented in [92]. A 1-bit coding diffusion metasurface having a metallic square rings resonator is proposed in [99], as shown in Fig. 10.

By utilising the particle swarm optimization algorithm in [96], the functionality of transmission and RCS reduction using metasurfaces has been realized. RCS is significantly reduced in the frequency range of 8.5–13.5 GHz by about 15 dB. In [100], a 3-bit metasurface is presented, utilizing split ring unit cells. The metasurface achieves a 10 dB reduction in RCS, specifically in the co-polarized configuration within an angle range of 0° to 30°. Fig. 11 illustrates the 3-bit coding metasurface design configuration described in the paper.

Using the discrete water recycle technique, [97] presents a 4-bit reflective coding metasurface with a polarization-insensitive unit cell for wideband RCS reduction. Similarly, in [101], the water cycle algorithm is employed for multi-bit coding element design, achieving 7 dB and 10 dB RCS reduction in the frequency ranges of 10–12 GHz and 10.5–11.5 GHz, respectively. Combining polarization conversion and binary coding for RCS reduction up to 125% is achieved in [67], utilising a search algorithm. A 3-bit random coding metasurface with eight elements is used in [98] to show RCS reduction in the 18.3–42.2 GHz frequency band. Using a coding diffusion metasurface and the random optimization algorithm, [102] achieves wideband RCS reduction and achieves a 10 dB RCS reduction in the frequency range of 8.6–22.5 GHz. In [103], a two-stage optimization technique for RCS reduction combines sequential search methodology with data-driven supervised learning. This method reduces the RCS by 10 dB and 15 dB in the frequency ranges of 14.8–37.2 GHz and 16.7–37 GHz respectively.

In [104], a coding diffused metasurface based on the ergodic algorithm and array factor is proposed for designing AMC blocks, 10 dB RCS reduction is achieved in the frequency range of 5.4–7.4 GHz, providing a bandwidth of 27.8% and offering a faster approach. An improved bandwidth of up to 69% is reported in [105] using a spiral track arrangement coding metasurface.

Matrix-type coding in [106] increases bandwidth by an additional 87%. A one-bit coding diffusion metasurface with greater bandwidth than CMS is shown in [107]. In [108], a non-planar coded diffusive metasurface in the frequency range of 6.4–30.1 GHz achieves a fractional bandwidth of 129%, demonstrating the increased bandwidth offered by non-planar structures. A new quick optimization approach with a low Q resonator is presented in [109] for effective coding metasurface and RCS reduction. The convolution of two separate coding surfaces serves as the foundation for the optimization approach, which improves the coding matrix's effectiveness and reduces the RCS in the frequency range of 5.8–21.5 GHz. In [95], a Pancharatnam-Berry phased coding polarizer is introduced to achieve a 10 dB reduction in RCS. This polarizer is designed to convert incident electromagnetic waves into cross-polarized waves through diffused scattering, operating effectively within the frequency range of 6–16 GHz. Using a checkerboard layout on a planar surface, an absorption and phase cancellation

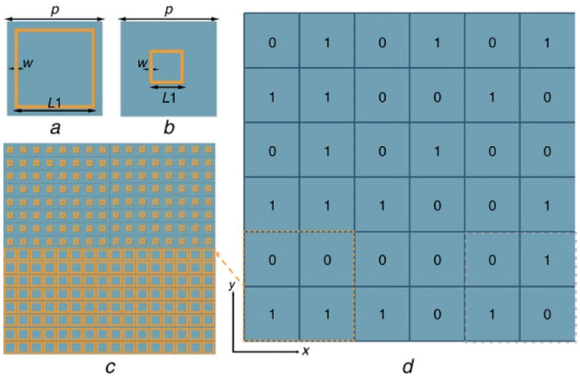


Fig. 10. Proposed ultrawideband 1-bit coding metasurface [99].

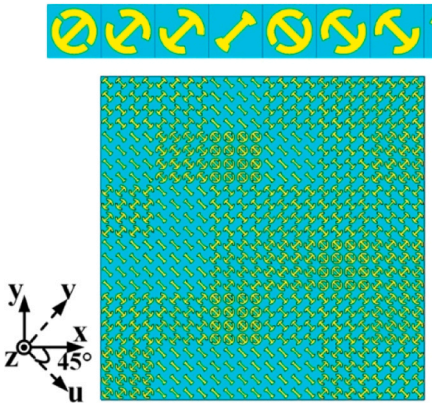


Fig. 11. 3-bit coding metasurface design with unit cell designs [100].

method is suggested in [109] to achieve a 20 dB RCS reduction in the wideband frequency range of 11.5–16 GHz.

The RCS reduction for flat metal targets has been the main emphasis of all the models thus far. However, in [110], flexible ultrathin coding metasurfaces with high optical transparency are used to achieve RCS reduction of cylindrical targets. The phased quantized coded metasurface is covered in [111] and [112], both of which make use of backscattering suppression methods. In [113], a conformal coding metasurface is proposed for the Ultra-Wideband (UWB) frequency range of 10.8–31.3 GHz, combining absorption, polarization conversion, and diffusion mechanisms. This design achieves a 10 dB reduction in RCS for both planar and conformal (up to 90°). A Pancharatnam-based 1-bit coded flexible metasurface is proposed in [77], utilizing the genetic algorithm and electromagnetic scattering principles. In the frequency ranges of 9.26–12.87 GHz and 14.84–19.35 GHz, this design achieves a 10 dB RCS reduction.

Coded metasurfaces can be designed using CMS, PGMS, PCMS, or a combination thereof. For RCS reduction and bandwidth enhancement, optimization techniques are employed in these design approaches of metasurface to get maximum RCS reduction. A consolidated summary of

α	0°	22.5°	45°	67.5°	90°	112.5°	135°	157.5°
Unit								
1-bit	0	–	–	–	1	–	–	–
2-bit	00	–	01	–	10	–	11	–
3-bit	000	001	010	011	100	101	110	111

Fig. 9. 1-, 2- and 3-bit coding sequence on metasurfaces using different sizes of unit cells [95].

all discussed models is given in the Table 4:

3.3.5. Reconfigurable metasurface

Passive metasurfaces are limited in their operation to specific frequency points and require more models for frequency adjustments. However, this limitation can be overcome by integrating external triggering circuits to achieve tunability. By incorporating stimuli-responsive materials that react to external parameters such as pressure, temperature, electric field, humidity, or light, the response of the metasurfaces can be altered. This enables dynamic adjustments and changes in functionality, leading to globally tuned metasurfaces.

Globally tuned metasurfaces can be acheived by utilizing materials such as graphene and liquid crystals, which can be externally controlled to modify the overall performance. Conversely, locally tuned metasurfaces aim to change the functional performance at the individual unit cell level. This can be achieved using components like pin diodes and varactor diodes, which enable the independent tuning of each unit cell.

3.3.5.1. Globally tuned. The concept of globally tuned metasurfaces is discussed in [115–117]. In [115], a tunable terahertz coding metasurface technique is introduced utilizing metallic patches embedded with vanadium. The functionality of this approach can be adjusted by utilizing the metallic-insulator transition of vanadium dioxide (VO2) at 68°C, enabling RCS reduction.

In [116], a tunable broadband RCS reduction technique is presented, combining the Salisbury screen with a high-index grating structure. The Salisbury screen incorporates graphene material, allowing for the tuning of surface resistance. Under normal incidence, the incoming wave is absorbed by the Salisbury screen, while the high-index grating structure reduces backward scattering by generating higher-order reflection

Table 4
Coding Metasurface Comparison.

Sr. No	Ref. No	Scattering Type	Optimization Method	a) RCS reduction frequency range b) Monostatic/Bistatic		Unit cell size	Array Size	Conformal Design
				Simulated Result	Measured Result			
1	[90]	Diffused	-	0.8–1.4 THz Monostatic/Bistatic	0.8–1.4 THz Monostatic/Bistatic	0.4λo x 0.4λo	36.7λo x 36.7λo	Yes
2	[92]	Diffused	-	0.88–1.38 THz Bistatic	0.88–1.38 THz Bistatic	0.14λo x 0.14λo	9.41λo x 9.41λo	No
3	[91]	Diffused	Particle Swarm Optimization	0.8–2 THz Monostatic/Bistatic	0.5–1.6 THz Monostatic/Bistatic	0.3λo x 0.3λo	25.2λo x 25.2λo	No
4	[93]	Polarization Conversion	Genetic algorithm + Coding element + Coding sequence optimization	12–24 GHz Monostatic	12–24 GHz Monostatic	0.2λo x 0.2λo	6.4λo x 6.4λo	No
5	[94]	Phase Cancellation	Particle Swarm Optimization	15–35 GHz Bistatic	15–35 GHz Bistatic	0.15λo x 0.15λo	6λo x 6λo	No
6	[99]	Diffused	-	8.01–22.76 GHz Monostatic	8.01–22.76 GHz Monostatic	0.16λo x 0.16λo	7.7λo x 7.7λo	No
7	[102]	Diffused	Random Optimization algorithm	8.6–22.5 GHz Monostatic/Bistatic	8.6–22.5 GHz Monostatic/Bistatic	0.17λo x 0.17λo	7.76λo x 7.76λo	No
8	[103]	Diffused	Data-driven supervised learning, sequential search Strategy + Direct EM design closure	14.8–37.2 GHz and 16.7–37 GHz Monostatic/Bistatic	14.8–37.2 GHz and 16.7–37 GHz Monostatic/Bistatic	0.3λo x 0.3λo	4.8λo x 4.8λo	No
9	[104]	Diffused	Ergodic algorithm	5.4–7.4 GHz Monostatic/Bistatic	5.57–7.37 GHz Monostatic/Bistatic	0.11λo x 0.11λo	7λo x 7λo	No
10	[114]	Phase Cancellation	Fast Optimization	5.8–21.5 GHz Monostatic	5.8–21.5 GHz Monostatic	0.12λo x 0.12λo	-	No
11	[101]	Diffused Scattering	Water cycle algorithm	10–12 GHz and 10.5–11.5 GHz Monostatic	10–12 GHz and 10.5–11.5 GHz Monostatic	0.26λo x 0.26λo	6.4λo x 6.4λo	No
12	[105]	Diffused	-	13.2–23.2 GHz Monostatic/Bistatic	12.2–23.4 GHz Monostatic/Bistatic	0.3λo x 0.3λo	14.4λo x 14.4λo	No
13	[107]	Diffused	Annealing algorithm	7–20 GHz Monostatic	7–20 GHz Monostatic	0.45λo x 0.45λo	7.5λo x 7.5λo	No
14	[106]	Polarization Conversion	Matrix-type random coding	6–15 GHz Monostatic/Bistatic	5.8–15.5 GHz Monostatic/Bistatic	0.35λo x 0.35λo	10.5λo x 10.5λo	No
15	[111]	Diffused	Phased quantized supercell	9–11 GHz Monostatic	9–11 GHz Monostatic	0.23λo x 0.23λo	8.4λo x 8.4λo	No
16	[96]	Destructive Interference	Particle swarm optimization	8.5–13.5 GHz Monostatic/Bistatic	8.5–13.5 GHz Monostatic/Bistatic	0.48λo x 0.48λo	11λo x 11λo	No
17	[97]	Diffused	Water cycle algorithm	15–40 GHz Monostatic	15–40 GHz Monostatic	0.46λo x 0.46λo	29λo x 29λo	No
18	[98]	Diffused scattering and polarization conversion	-	14.4–48.5 GHz Monostatic	1842.2 GHz Monostatic	0.42λo x 0.42λo	26.6λo x 26.6λo	No
19	[67]	Diffused scattering and polarization conversion	Group search optimization	5.1–22.1 GHz Monostatic/Bistatic	4.8–22.8 GHz Monostatic	0.36λo x 0.36λo	14.5λo x 14.5λo	No
20	[108]	Destructive Interference	Discrete particle swarm optimization	6.4–30.1 GHz Monostatic/Bistatic	6.4–29.6 GHz Monostatic/Bistatic	0.48λo x 0.48λo	13.6λo x 13.6λo	No
21	[95]	Diffused scattering and polarization conversion	-	6.9–14.5 GHz Monostatic	6.9–14.5 GHz Monostatic	0.20λo x 0.20λo	6.97λo x 6.97λo	No
22	[109]	Absorptive and Phase Cancellation	-	11.5–16 GHz Monostatic	11.5–16 GHz Monostatic	0.23λo x 0.34λo	11.5λo x 11.5λo	No
23	[113]	Absorption and Diffusion	Optimized sequence	10.8–31.3 GHz Monostatic	-	0.21λo x 0.21λo	-	Yes
24	[77]	Polarization Conversion	Genetic algorithm + Planar array pattern	9.61–12.18 and 14.60–18.61 GHz Monostatic/Bistatic	9.61–12.18 and 14.60–18.61 GHz Monostatic/Bistatic	0.3λo x 0.3λo	8λo x 8λo	Yes

beams, effectively reducing RCS.

3.3.5.2. Locally tuned. The metasurface possesses the capability to alter reflection characteristics at the unit cell level. To enact a binary-coded locally tuned metasurface, a pin diode is integrated into each unit cell. Utilizing a matrix method enables the accomplishment of multiple functionalities through optimization of the metasurface. A Field-Programmable Gate Array (FPGA)-based controller is situated at the back of the metasurface, allowing for real-time control of each unit cell. The controller is connected via fixable windings, facilitating the execution of real-time control operations [118].

Metamaterial research has advanced significantly, enabling precise manipulation of electromagnetic wave fields. However, programmable metasurfaces often necessitate manual intervention to switch between different functionalities. To address this limitation, metamaterials have been developed to self-adaptively reprogram themselves based on surrounding sensing. By incorporating an autonomous sensing feedback system, the metamaterial can dynamically adjust its electromagnetic functioning. In [119], a three-axis gyroscope is integrated into a motion-smart sensitive metasurface, allowing it to adaptively change its electromagnetic radiation by incorporating different rotations. Additionally, a software switch is introduced to facilitate switching between single and multiple-beam steering modes, as presented in Fig. 12.

In [120], a programmable multifunctional reconfigurable metasurface is proposed that enable real-time control of electromagnetic waves by allowing changes in the digital coding sequence

3.3.6. Time varying metasurface

The previously discussed metasurfaces mainly concentrated on modifying the reflection of waveforms while keeping the frequency content constant. However, a novel technique has been introduced where the incident spectrum is dispersed across various frequency bands, thereby enhancing the invisibility of the target. In [121], this technique is implemented by incorporating spectrum technology and time-domain modulation. In [122], the Lorentz concept is dismissed in favor of achieving time-varying characteristics, giving rise to the concept of time-varying metasurfaces. Additionally, transverse temporal modulation of surface impedance is utilized in graded metasurfaces to attain desired properties [123].

In [124], Huygens' metasurface is introduced as a space-time modulated structure, which eliminates the need for spatial-temporal traveling waves. The variation in permittivity is translated into Lorentz susceptibility parameters through a set of second-order differential equations. Numerical modeling is carried out using a finite-difference time-domain (FDTD) approach. An explicit time difference technique is applied to solve the gap, and the outcomes are incorporated into the Yee cell-based propagation region.

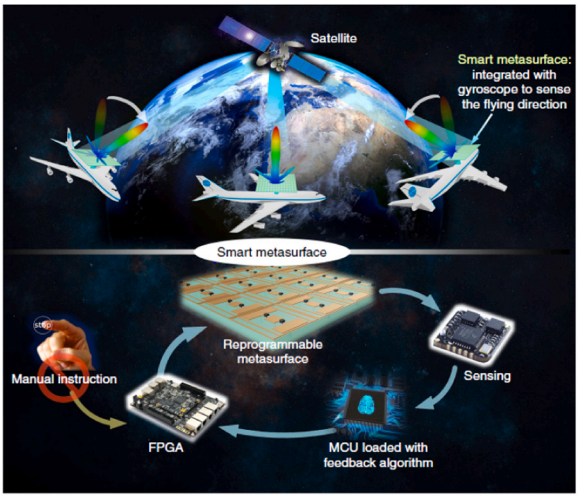


Fig. 12. Schematics of self-adaptive programmable metasurface without any manual instructions [119].

In [125,126], graphene-based time-varying metasurfaces are presented, allowing for the manipulation of incident signals in the terahertz regime. In [125], a graphene micro-ribbon array is discussed, where the Fermi level can be altered through graphene doping, resulting in time-varying changes that allow for active regulation of amplitude and phase reflection. The mechanism used to regulate and alter light properties resembles Doppler-like shifts.

Proposed work in [127], the utilization of PEC and Perfect Magnetic Conductor (PMC) based unit cells, along with pseudo-random time modulation. This approach is part of camouflaging metasurface technology, enabling control over the metal surface. The control of the metal surface using a digital coding sequence is further explored in [121]. Through temporal modulation of incident waves on the metasurface, nonlinearity is induced, enabling control over amplitude and phase modulation. A novel coding sequence of meta-atoms is proposed in [128] for different modulations in an asynchronous space-time coding digital metasurface. This work aims to convert phase discontinuities into different frequency, enhancing the functionality and performance of the metasurface, as depicted in Fig. 13.

3.4. Absorptive metasurface

In this section, the focus is on metasurfaces designed to reduce RCS through absorption. Absorptive metasurfaces must eliminate both reflection and transmission to effectively absorb incident waves. Achieving this requires matching the impedance of the absorber layer to the impedance of free space to fulfill the no-reflection requirement. Increasing the thickness of the absorbing layer or creating an electromagnetic response that uses the electric and magnetic fields to dissipate the incident wave are two ways to reduce transmission. The objective of the Metamaterial absorber presented in [129] is to achieve high absorption of incident waves. Another approach involves resistive component-coupled elements, as demonstrated in [130,131], which achieve nearly 10 dB RCS reduction. In [132], an ultrathin Frequency Selective Surface (FSS) broadband one-layer absorber is introduced, utilizing four treble square resistive loops to reduce RCS to the desired level.

While several techniques were presented in reference [133] for unit cell design focusing on conformal patches, this technique employs the FSS screen with RF absorber to achieve the desired RCS reduction. This approach proves effective for addressing limited RCS reduction bandwidth and poor antenna performance issues, but the height proves to be the constraint in the design. A microwave absorber based FSS design is introduced in [134], comprising a single layer FSS with four lumped resistors operating within the range of 14.2–30.3 GHz, demonstrating sufficient absorption capabilities. However, the RCS reduction is not specified for this unit cell design.

In [135], a unit cell-based design achieves 88% absorption at a frequency of 11.5 GHz. Similarly, a high-performance absorber with 99.8% absorption and an 8% fractional bandwidth is proposed in [136]. Furthermore, [137] introduces a metallic cube designed specifically for RCS reduction; it exhibits no reflection or transmission at 10 GHz. These works highlight various approaches to designing metasurfaces that effectively absorb incident waves to reduce RCS.

In [138], the functionality of an absorber is achieved by utilizing surface current distribution. An ultra-thin absorber operating in the X-band frequency range is proposed, featuring concentric circular split rings. Whereas in [139], a triple X-band absorber is introduced as shown in Fig. 14, its absorber utilizes split rings and incorporates a dual-polarized band-pass band and a notched FSS configuration.

The surface current on the elements of the wideband circuit analog absorber proposed in [140] is meant to be antiparallel to that of the ground plane. This absorber achieves a fractional bandwidth of 114.4%.

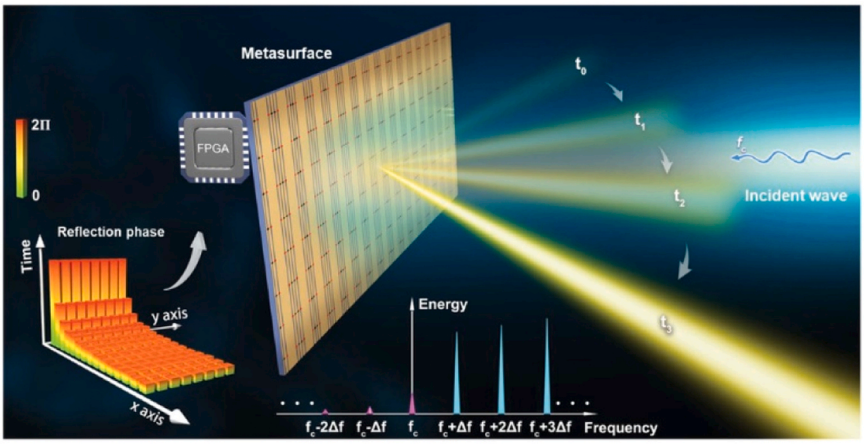


Fig. 13. Illustration of asynchronous space-time coding metasurface by the change of the biasing voltage of varactor diode [128].

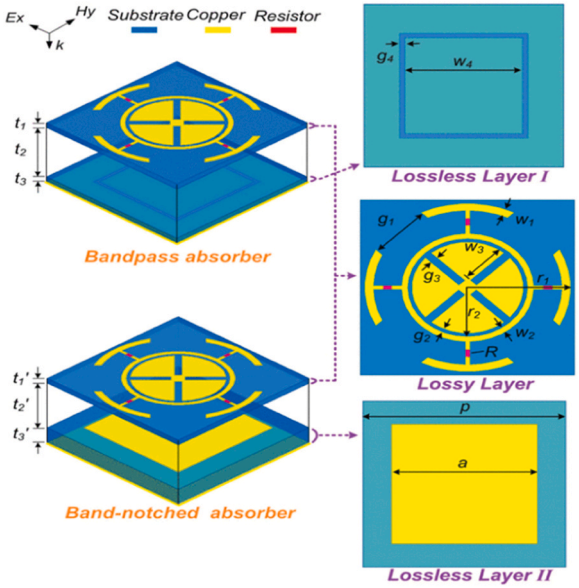


Fig. 14. Proposed unit cell of dual-polarized band pass band notched FSS absorber [139].

Wideband RCS reduction absorbers with band-notched elements are presented in [137–139]. For a wide frequency range, these designs aim to lessen RCS over a while by incorporating band-notched features. In [141], a stand-up resistive film patch array is introduced, which utilizes multiple standing wave modes of excitation to achieve ultra-wideband absorption.

In [142], a square-ringed ultrathin metamaterial absorber is presented. This model consists of several resonators connected in parallel by short-circuit transmission lines and coupling capacitors. Equivalent circuit-based model designs are discussed in [143–145]. In [145], a bandwidth of 0.68 THz is achieved using graphene-based material. In [146], an inverse synthetic aperture radar (ISAR) imaging technique and high-frequency approximation are utilized to analyze the scattering mechanisms of elliptic shapes. To mitigate specular reflection and edge diffraction effects, FSS absorbers and tapered resistive sheets are employed. The proposed [147] reflective metasurface, featuring a frequency-selective surface with a resistive-loaded lossy layer, aims at reducing RCS in the S and C bands. It achieves high gain and RCS reduction by generating a parallel beam that can be transmitted through a transparent window.

In [148], a design aims to achieve a 20 dB reduction using planar and conformal design, featuring four metallic patches and four lumped resistors within the frequency range of 13.42–22.66 GHz. A metamaterial comprising a 16×16 unit cell structure is utilized, with an FR-4 substrate positioned on the top layer. The design details can be found in Fig. 15.

In the context of multiband Absorbing Magnetic Composite-based absorbers, the introduction of magnetic loading has been shown to enhance the bandwidth, as discussed in [149,150]. In [151], a sugarcane bagasse-based composite absorber is presented, which leverages the effect of a FSS for the enhancement of absorption characteristics. The combination of coding metasurface and metamaterial absorbers is explored in [152], demonstrating that the joint utilization of these two technologies can increase the RCS bandwidth and result in lessening the RCS compared to individual metamaterial absorbers. An enhanced gain antenna with band pass FSS is proposed in [153], a quasi-Fabry-Perot cavity is created between the FSS and the antenna ground. For enhanced gain, the FSS introduces slight phase compensation for the oblique transmitting wave. A Fabry-Perot cavity antenna is proposed in [154] for radiation enhancement and monostatic RCS reduction. In transmission mode, the antenna achieves beam deflection and gain enhancement while maintaining a low profile. A metallic ring with resistors is employed as an absorptive frequency-selective surface (AFSS), in conjunction with a dual-sided PRS, to achieve these improvements.

The models presented above primarily focus on reducing the RCS of flat metal targets passively. However, in [155], the focus shifts to reducing the RCS of antennas specifically for oblique incidences. In [156], an active liquid crystal metasurface tunable absorber is proposed. This model offers frequency tunability of up to 4%, allowing for adjustable absorption characteristics. In [157], a frequency-selective surface absorber with a tapered resistive sheet is provided, dividing the entire angular range from 0° to 90° degrees into three distinct sections. RCS reduction is reported within the 0°-10° and 30°-85° range. In the work proposed in [158], the reduction of RCS in reflect arrays is achieved using a controllable model. While out-of-band scattering is reduced, the conductive surface in-band phase profile directly contributes to the far-field beam. A low-profile absorber for ultrawideband applications is presented in [159]; for monostatic and bistatic RCS reduction, this metasurface incorporates a printed lossy capacitive surface. In [160], the reduced thickness design with high angular stability is proposed for bistatic RCS reduction. Whereas in [161], a polarized-insensitive miniaturized band-notched absorber with a resistive top layer is introduced. This work focuses on achieving angular stability and small lateral dimensions while maintaining efficient absorption and band-notched characteristics. The absorber's performance is intended to remain constant over a broad range of incidence angles and polarization states. A comparative analysis in Table 5 proposes the models discussed for RCS reduction using absorptive materials

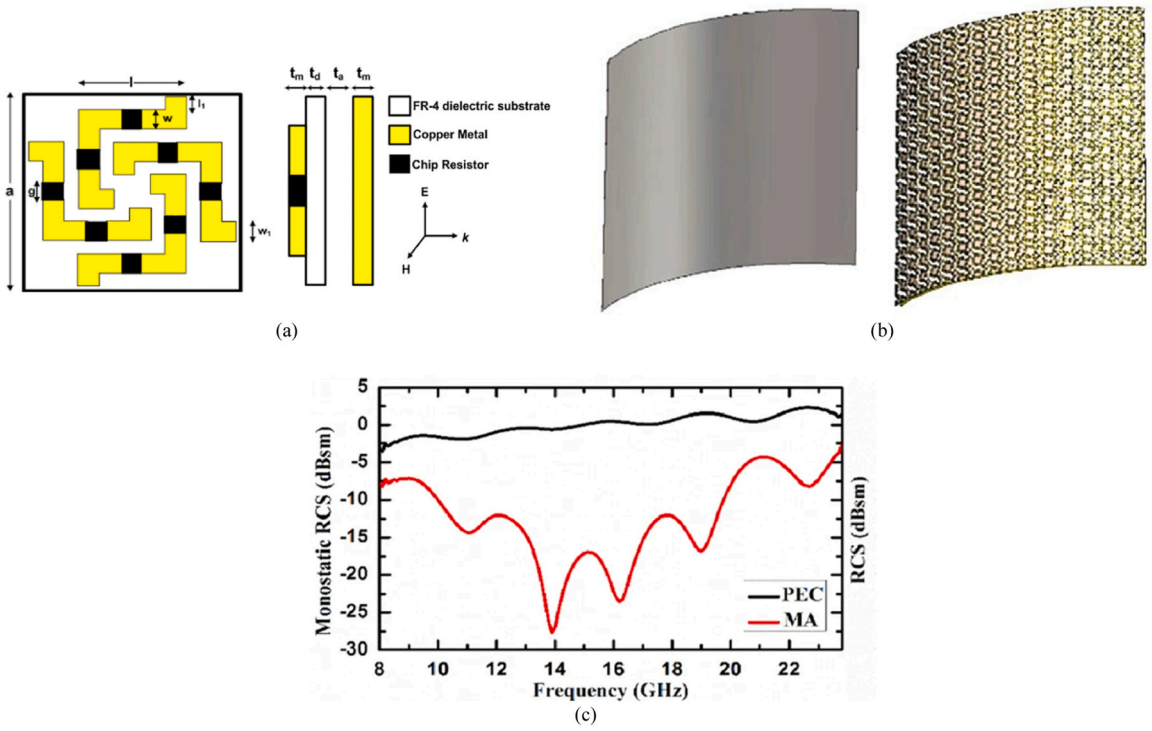


Fig. 15. (a) Proposed unit cell geometry absorber top view and side view, (b) 3D view of the cylindrically bent design of metasurface [148].

4. Future research direction

In future research, emphasis should be placed on developing phase change principles that maintain the original electromagnetic (EM) field distribution while achieving a broad bandwidth. Miniaturizing resonators to deep subwavelength scales presents a significant challenge, alongside exploring innovative strategies to reduce bulk profile thickness at low microwave frequencies while ensuring optimal RCS reduction performance.

Intelligent metasurfaces, incorporating AI-powered designs or sensor-integrated platforms, are poised to shape the upcoming era. This transition underscores the increasing importance of sensing and recognition capabilities in managing electromagnetic characteristics and executing complex computing tasks. Coding metasurfaces are anticipated to play a pivotal role in this context, potentially combined with programmable metasurfaces to drive advancements in wireless communication and radar systems.

Extensive research has been conducted in the field of RCS reduction, yet several unresolved issues persist. Some of the challenges include:

- Targets designed with absorptive metasurfaces can be detected by infrared radars due to heat emission, a research area that remains unexplored. To conceal targets effectively, they must be resistant to infrared radar detection.
- Most researchers have focused on monostatic RCS reduction using periodic structures. However, aperiodic structures may affect RCS reduction efficiency, especially at oblique incidences. Therefore, combining periodic and aperiodic patterns could yield more favorable results.
- The requirement for a phase difference of $180\pm37^{\circ}$ between two unit cells, as commonly seen in coding 1-bit metasurfaces, limits unit cell design flexibility. Efforts should be made to design structures that do not rely on this criterion.
- The substrate plays a crucial role in RCS reduction systems. While thicker substrates are beneficial for low frequencies, enhancing stealth applications, they also increase structure bulkiness and resistance to conformal applications. Thus, a tradeoff between substrate thickness and operating frequency is necessary.
- Passive RCS reduction techniques are typically effective for single target scenarios but may need adaptation for multiple targets.
- Addressing these challenges will advance the field of RCS reduction and contribute to more effective stealth and radar technologies.

Scattering-based metasurfaces aimed at reducing RCS bandwidth can be achieved through various approaches. These include the utilization of multi-resonant elements [55], elements that is designed to suppress surface waves, and non-resonant elements [163]. Additionally, optimization strategies highlighted in [61,107] have demonstrated effectiveness in improving RCS reduction bandwidth. A recent study [164] introduces a design for a low-scattering metasurface using a Machine Learning-based framework. By employing a combination of global search and local tweaking of the direct metasurface, this concept optimizes AMC cells to achieve a broader bandwidth. Moreover, this technology has the potential to enhance the bandwidth capabilities of other types of metasurfaces as well.

The available literature indicates that most research efforts have primarily focused on achieving monostatic bandwidth for RCS reduction. Yet, it is found that the monostatic mode bandwidth cannot be replicated in the bistatic mode. The discrepancy results from the fact that, in contrast to normal incidence, as explained in Huygens metasurfaces, the surface impedance of the metasurface changes when oblique angles are involved [165]. Another study [166] further emphasizes that inhomogeneous metasurfaces operating at oblique incidence suffer from performance degradation. Therefore, it becomes crucial to address the angular dependence and ensure consistent performance across different angles. One promising approach to tackling this challenge is utilizing metaatoms that demonstrate reduced multi-polar mode coupling [166]. These findings highlight the existence of a substantial research area in the field of bistatic RCS reduction. A wide bandwidth can only be attained by carefully considering a metasurface design, element spacing, size, and thickness. Although researchers have extensively studied these parameters for various electromagnetic problems,

Table 5
Absorptive Metasurface Comparison.

Sr. No	Ref. No	a) RCS reduction frequency range b) Monostatic/Bistatic		Unit cell size	Array Size	Conformal Design
		Simulated Result	Measured Result			
1	[129]	8–18 GHz Monostatic	8–18 GHz Monostatic	0.56λo x 0.56λo	6.9λo x 6.9λo	No
2	[131]	8–18 GHz Monostatic	N/A	0.85λo x 0.85λo	1.65λo x 1.65λo	No
3	[132]	10.7–29 GHz Monostatic	N/A	0.28λo x 0.28λo	N/A	No
4	[133]	6–12 GHz Monostatic	N/A	0.304λo x 0.304λo	N/A	No
5	[137]	5.22, 9.96, 7.44 and 10.48 GHz Monostatic/Bistatic	5.258, 10.02, 7.518 and 10.494 GHz Monostatic/Bistatic	0.47λo x 0.47λo	6.3λo x 6.3λo	No
6	[138]	7.85–12.25 GHz Monostatic/Bistatic	8.08–12.12 GHz Monostatic/Bistatic	0.238λo x 0.238λo	7.8λo x 7.8λo	No
7	[140]	5.1–18.08 GHz Monostatic	4.96–18.22 GHz Monostatic	0.502λo x 0.502λo	7λo x 7λo	No
8	[139]	3.9–26.2 GHz Monostatic	3.9–26.2 GHz Monostatic	0.602λo x 0.602λo	12λo x 12λo	No
9	[162]	2.12–4.15 GHz and 6.08–9.58 GHz Monostatic	2.12–4.15 GHz and 6.08–9.58 GHz Monostatic	0.380λo x 0.380λo	5.7λo x 5.7λo	No
10	[142]	6.14 GHz Monostatic	6.14 GHz Monostatic	0.204λo x 0.204λo	-	No
11	[143]	5.9 GHz Monostatic	5.9 GHz Monostatic	0.39λo x 0.39λo	3.5λo x 3.5λo	No
12	[144]	1.98–9 GHz (Single layer) and 1.07–9.7 GHz (double layer) Monostatic/Bistatic	1.98–9 GHz (Single layer) and 1.07–9.7 GHz (double layer) Monostatic/Bistatic	0.2745λo x 0.2745λo and 0.302λo x 0.302λo	-	No
13	[147]	2.3–8.55 GHz Monostatic	2.3–8.55 GHz Monostatic	0.16λo x 0.16λo	1.85λo x 1.85λo	No
14	[153]	5–5.33 GHz, 9–13.4 GHz (TE Pol) 8.4–13.5 GHz (TM Pol) Monostatic/Bistatic	5–5.33 GHz, 9–13.4 GHz (TE Pol) 8.4–13.5 GHz (TM Pol) Monostatic/Bistatic	0.2λo x 0.2λo	1λo x 1λo	No
15	[154]	4–16 GHz (8.5 dB RCSR) Monostatic	4–16 GHz (8.5 dB RCSR) Monostatic	0.2λo x 0.2λo	1.4λo x 1.4λo	No
16	[157]	1.3–2 GHz Monostatic	1.3–2 GHz Monostatic	0.108λo x 0.108λo	1.3λo x 2.16λo	No
17	[160]	4.893–5.55 GHz Monostatic/Bistatic	4.893–5.55 GHz Monostatic/Bistatic	0.7λo x 0.7λo	5.3λo x 5.3λo	No
18	[159]	3–12 GHz Monostatic/Bistatic	3–12 GHz Monostatic/Bistatic	0.24λo x 0.24λo	1.92λo x 1.92λo	No
19	[161]	2.48–5.23 GHz and 7.68–12.26 GHz Monostatic	2.48–5.23 GHz and 7.68–12.26 GHz Monostatic	0.2457λo x 0.2457λo	14.5λo x 14.5λo	No
20	[146]	1.35–4.9 GHz Bistatic	1.35–4.9 GHz Bistatic	0.09λo x 0.09λo	2.27λo x 2.27λo	Yes
21	[148]	13.42–22.6 GHz Monostatic/Bistatic	13.42–22.6 GHz Monostatic/Bistatic	0.45λo x 0.45λo	7.72λo x 7.72λo	Yes

the relationship between RCS reduction and array size has not been thoroughly investigated in the context of antennas. However, studies on phased arrays [167] and reflect arrays [168] have shown that there is indeed a correlation between array size and bandwidth. This implies that examining the relationship between RCS reduction and array size may increase bandwidth. Therefore, further research and exploration in this direction holds promise for achieving broader bandwidths in RCS reduction applications.

Mitigating the mutual coupling effect and refining prediction models for array bandwidth offer enhanced effectiveness of RCS reduction metasurfaces. As radar advancements demand higher reductions in RCS, adapting existing models to achieve greater reductions becomes essential. This may involve developing algorithms using artificial intelligence for unit cell design and exploring conformal designs of metasurfaces to meet evolving requirements in practical applications.

5. Conclusion

This paper provides a comprehensive discussion of various techniques and advancements in reducing RCS, with a specific focus on metasurfaces. It begins by presenting fundamental techniques of absorption and scattering for RCS reduction, along with shaping and RAM as methods for reducing RCS. The paper then delves into a detailed review of RCS reduction using metasurfaces, examining both passive and active configurations and thoroughly exploring their profile, frequency range, technique, and design complexity. The authors comprehensively analyze the current state of metasurface-based RCS reduction, discussing strengths, limitations, and identifying gaps in current research. Moreover, they highlight areas that require further investigation, offering valuable insights into potential avenues for future research using metasurfaces. Overall, this paper offers an in-depth exploration of RCS reduction techniques, emphasizing the planar and conformal design of metasurfaces, and serves as a valuable resource for researchers and

practitioners in the field.

Declaration of Competing Interest

The authors declare that they have no known competing financial interests or personal relationships that could have appeared to influence the work reported in this paper.

Acknowledgement

This work was supported in part by the Universiti Malaya (UM) under Grant GPF008A-2023 and United Arab Emirates University (UEAU) under Grant IF055-2021.

References

[1] W.M. Dorsey, V. Monebhurrun, E. Mokole, IEEE Standard 1502: Standardization of Radar Cross-Section Test Procedures [Stand on Standards], IEEE Antennas Propag. Mag. 64 (2) (2022) 73–78.
[2] E.F. Knott, J.F. Schaeffer, M.T. Tulley, Radar cross section, SciTech Publishing, 2004.
[3] T. Dobrenz, A. Spadoni, M. Jorgensen, Aviation archeology of the Horten 229 v3 aircraft, 10th AIAA Aviat. Technol., Integr., Oper. (ATIO) Conf. (2010).
[4] P.Y. Ufimtsev, Elementary edge waves and the physical theory of diffraction, Electromagnetics 11 (2) (1991) 125–160.
[5] U. Lockheed, Lockheed U-2. Ultim. Collect. UFOs (2012) 99.
[6] N. Yu, F. Capasso, Flat optics with designer metasurfaces, Nat. Mater. 13 (2) (2014) 139–150.
[7] A.K. Iyer, A. Alu, A. Epstein, Metamaterials and metasurfaces—historical context, recent advances, and future directions, IEEE Trans. Antennas Propag. 68 (3) (2020) 1223–1231.
[8] S.S. Bukhari, J. Vardaxoglou, W. Whittow, A metasurfaces review: definitions and applications, Appl. Sci. 9 (13) (2019) 2727.
[9] H.-T. Chen, A.J. Taylor, N. Yu, A review of metasurfaces: physics and applications, Rep. Prog. Phys. 79 (7) (2016) 076401.
[10] M. Chen, et al., Huygens' metasurfaces from microwaves to optics: a review, Nanophotonics 7 (6) (2018) 1207–1231.
[11] Y. Fan, et al., Recent developments of metamaterials/metasurfaces for RCS reduction, EPJ Appl. Metamater. 6 (2019) 15.
[12] R. Zaker, A. Sadeghzadeh, Passive techniques for target radar cross section reduction: A comprehensive review, Int. J. RF Microw. Comput. -Aided Eng. 30 (11) (2020) e22411.
[13] R. Maggiora, et al., An innovative harmonic radar to track flying insects: the case of Vespa velutina, Sci. Rep. 9 (1) (2019) 11964.
[14] S.-L. Jeng, W.-H. Chieng, H.-P. Lu, Estimating speed using a side-looking single-radar vehicle detector, IEEE Trans. Intell. Transp. Syst. 15 (2) (2013) 607–614.
[15] W.-L. Guo, et al., Transmission–reflection-selective metasurface and its application to RCS reduction of high-gain reflector antenna, IEEE Trans. Antennas Propag. 68 (3) (2019) 1426–1435.
[16] K. Vinoy, R. Jha, Trends in radar absorbing materials technology, Sadhana 20 (1995) 815–850.
[17] G. Rao, S. Mahulikar, Integrated review of stealth technology and its role in airpower, Aeronaut. J. 106 (1066) (2002) 629–642.
[18] R. Francis, The development of blue steel, Aeronaut. J. 68 (641) (1964) 303–322.
[19] G. Bao, J. Lai, Optimal shape design of a cavity for radar cross section reduction, SIAM J. Control Optim. 52 (4) (2014) 2122–2140.
[20] G. Peixoto, et al., Radar absorbing material (RAM) and shaping on radar cross section reduction of dihedral corners. SBMO/IEEE MTT-S International Conference on Microwave and Optoelectronics, 2005, IEEE, 2005.
[21] Swandic, J., Bandwidth limits and other considerations for monostatic RCS reduction by virtual shaping. 2004, Naval surface warfare center carderock DiV bethesda md survivability ….
[22] Saville, P., Review of radar absorbing materials. 2005, Defence Research and Development Atlantic Dartmouth (Canada).
[23] Z. Ali, et al., Design of Microwave Pyramidal Absorber for Semi Anechoic Chamber in 1 GHz~ 20 GHz range, Int. J. Wirel. Microw. Technol. 10 (2) (2020) 22–29.
[24] B. Sweetman, Stealth aircraft-history, technology and outlook. in Turbo Expo: Power for Land, Sea, and Air, Citeseer, 1990.
[25] J.-P. Berenger, A perfectly matched layer for the absorption of electromagnetic waves, J. Comput. Phys. 114 (2) (1994) 185–200.
[26] Salisbury, W.W., Absorbent body for electromagnetic waves. 1952, Google Patents.
[27] B. Chambers, A. Tennant, Optimised design of Jaumann radar absorbing materials using a genetic algorithm, IEE Proc. -Radar, Sonar Navig. 143 (1) (1996) 23–30.
[28] M. Selvanayagam, G.V. Eleftheriades, Discontinuous electromagnetic fields using orthogonal electric and magnetic currents for wavefront manipulation, Opt. Express 21 (12) (2013) 14409–14429.
[29] J.P. Wong, M. Selvanayagam, G.V. Eleftheriades, Design of unit cells and demonstration of methods for synthesizing Huygens metasurfaces, Photonics Nanostruct. -Fundam. Appl. 12 (4) (2014) 360–375.
[30] C. Pfeiffer, A. Grbic, Metamaterial Huygens' surfaces: tailoring wave fronts with reflectionless sheets, Phys. Rev. Lett. 110 (19) (2013) 197401.
[31] A. Epstein, G.V. Eleftheriades, Shielded perfect reflectors based on omega-bianisotropic metasurfaces. 2017 International Workshop on Antenna Technology: Small Antennas, Innovative Structures, and Applications (iWAT), IEEE, 2017.
[32] M. Selvanayagam, G.V. Eleftheriades, Polarization control using tensor Huygens surfaces, IEEE Trans. Antennas Propag. 62 (12) (2014) 6155–6168.
[33] C. Pfeiffer, A. Grbic, Bianisotropic metasurfaces for optimal polarization control: Analysis and synthesis, Phys. Rev. Appl. 2 (4) (2014) 044011.
[34] N. Yu, et al., Light propagation with phase discontinuities: generalized laws of reflection and refraction, science 334 (6054) (2011) 333–337.
[35] S. Sun, et al., High-efficiency broadband anomalous reflection by gradient meta-surfaces, Nano Lett. 12 (12) (2012) 6223–6229.
[36] S. Sun, et al., Gradient-index meta-surfaces as a bridge linking propagating waves and surface waves, Nat. Mater. 11 (5) (2012) 426–431.
[37] H. Chen, et al., A wideband deflected reflection based on multiple resonances, Appl. Phys. A 120 (2015) 287–291.
[38] Y. Li, et al., Achieving wideband polarization-independent anomalous reflection for linearly polarized waves with dispersionless phase gradient metasurfaces, J. Phys. D: Appl. Phys. 47 (42) (2014) 425103.
[39] H. Umair, et al., Tilted beam Fabry–Perot antenna with enhanced gain and broadband low backscattering, Electronics 10 (3) (2021) 267.
[40] M. Pu, et al., Broadband anomalous reflection based on gradient low-Q meta-surface, AIP Adv. 3 (5) (2013) 052136.
[41] Y. Cheng, et al., An ultra-thin dual-band phase-gradient metasurface using hybrid resonant structures for backward RCS reduction, Appl. Phys. B 123 (2017) 1–6.
[42] Q. Zheng, et al., Wideband, wide-angle coding phase gradient metasurfaces based on Pancharatnam-Berry phase, Sci. Rep. 7 (1) (2017) 43543.
[43] Y. Li, et al., Wideband radar cross section reduction using two-dimensional phase gradient metasurfaces, Appl. Phys. Lett. 104 (22) (2014) 221110.
[44] Y. Azizi, M. Soleimani, S.H. Sedighy, Ultra-wideband radar cross section reduction using amplitude and phase gradient modulated surface, J. Appl. Phys. 128 (20) (2020) 205301.
[45] H. Umair, et al., Fabry-Perot antenna employing artificial magnetic conductors and phase gradient metasurface for wideband monostatic RCS reduction and high gain tilted beam radiation, IEEE Access 9 (2021) 66607–66625.
[46] J. Chen, et al., Reduction of radar cross section based on a metasurface, Prog. Electromagn. Res. 146 (2014) 71–76.
[47] W. Zhang, et al., Wideband RCS reduction of a slot array antenna using phase gradient metasurface, IEEE Antennas Wirel. Propag. Lett. 17 (12) (2018) 2193–2197.
[48] M. Paquay, et al., Thin AMC structure for radar cross-section reduction, IEEE Trans. Antennas Propag. 55 (12) (2007) 3630–3638.
[49] M.E. de Cos, Y. Alvarez-Lopez, F.L.H. Andres, A novel approach for RCS reduction using a combination of artificial magnetic conductors, Prog. Electromagn. Res. 107 (2010) 147–159.
[50] Y. Fu, Y. Li, N. Yuan, Wideband composite AMC surfaces for RCS reduction, Microw. Opt. Technol. Lett. 53 (4) (2011) 712–715.
[51] J.C.I. Galarregui, et al., Broadband radar cross-section reduction using AMC technology, IEEE Trans. Antennas Propag. 61 (12) (2013) 6136–6143.
[52] W. Chen, C.A. Balanis, C.R. Birtcher, Checkerboard EBG surfaces for wideband radar cross section reduction, IEEE Trans. Antennas Propag. 63 (6) (2015) 2636–2645.
[53] W. Chen, C.A. Balanis, C.R. Birtcher, Dual wide-band checkerboard surfaces for radar cross section reduction, IEEE Trans. Antennas Propag. 64 (9) (2016) 4133–4138.
[54] A.Y. Modi, et al., Novel design of ultrabroadband radar cross section reduction surfaces using artificial magnetic conductors, IEEE Trans. Antennas Propag. 65 (10) (2017) 5406–5417.
[55] D. Sang, et al., Design of checkerboard AMC structure for wideband RCS reduction, IEEE Trans. Antennas Propag. 67 (4) (2019) 2604–2612.
[56] S.H. Kim, Y.J. Yoon, Wideband radar cross-section reduction on checkerboard metasurfaces with surface wave suppression, IEEE Antennas Wirel. Propag. Lett. 18 (5) (2019) 896–900.
[57] J. MV, A. Pradeep, Low. RCS Patch Antenna Based Meand. Line Checkerboard (2023).
[58] J. Su, et al., A novel checkerboard metasurface based on optimized multielement phase cancellation for superwideband RCS reduction, IEEE Trans. Antennas Propag. 66 (12) (2018) 7091–7099.
[59] R. Zaker, A. Sadeghzadeh, Wideband radar cross section reduction using a novel design of artificial magnetic conductor structure with a triple-layer chessboard configuration, Int. J. RF Microw. Comput. -Aided Eng. 29 (2) (2019) e21545.
[60] A.Y. Modi, et al., New class of RCS-reduction metasurfaces based on scattering cancellation using array theory, IEEE Trans. Antennas Propag. 67 (1) (2018) 298–308.
[61] A. Murugesan, K.T. Selvan, On further enhancing the bandwidth of wideband RCS reduction checkerboard metasurfaces using an optimization algorithm, Int. J. RF Microw. Comput. -Aided Eng. 31 (7) (2021) e22686.
[62] A. Murugesan, D. Natarajan, K.T. Selvan, Low-cost, wideband checkerboard metasurfaces for monostatic RCS reduction, IEEE Antennas Wirel. Propag. Lett. 20 (4) (2021) 493–497.

[63] A.Y. Modi, et al., Metasurface-based method for broadband RCS reduction of dihedral corner reflectors with multiple bounces, IEEE Trans. Antennas Propag. 68 (3) (2019) 1436–1447.
[64] Z. Zhao, X. Li, G. Dong, Wideband RCS reduction based on hybrid checkerboard metasurface, Sensors 23 (8) (2023) 4054.
[65] W. Chen, et al., Cylindrically curved checkerboard surfaces for radar cross-section reduction, IEEE Antennas Wirel. Propag. Lett. 17 (2) (2018) 343–346.
[66] M.K.T. Al-Nuaimi, et al., Wideband Radar Cross Section Reduction Using Parabolic Phased Metasurfaces, IEEE Antennas and Wireless Propagation Letters, 2023.
[67] M. Akbari, et al., Superbroadband diffuse wave scattering based on coding metasurfaces: Polarization conversion metasurfaces, IEEE Antennas Propag. Mag. 61 (2) (2019) 40–52.
[68] H. Chen, et al., Ultra-wideband polarization conversion metasurfaces based on multiple plasmon resonances, J. Appl. Phys. 115 (15) (2014) 154504.
[69] W. Jiang, Y. Xue, S.-X. Gong, Polarization conversion metasurface for broadband radar cross section reduction, Prog. Electromagn. Res. Lett. 62 (2016) 9–15.
[70] Y. Jia, et al., Broadband polarization rotation reflective surfaces and their applications to RCS reduction, IEEE Trans. Antennas Propag. 64 (1) (2015) 179–188.
[71] H. Sun, et al., Broadband and broad-angle polarization-independent metasurface for radar cross section reduction, Sci. Rep. 7 (1) (2017) 1–9.
[72] Y. Jia, et al., A dual-patch polarization rotation reflective surface and its application to ultra-wideband RCS reduction, IEEE Trans. Antennas Propag. 65 (6) (2017) 3291–3295.
[73] E. Ameri, S.H. Esmaeli, S.H. Sedighy, Ultra wideband radar cross section reduction by using polarization conversion metasurfaces, Sci. Rep. 9 (1) (2019) 478.
[74] J.J. Yang, et al., Broadband polarization conversion metasurface based on metal cut-wire structure for radar cross section reduction, Materials 11 (4) (2018) 626.
[75] H. Rajabalipanah, A. Abdolali, Ultrabroadband monostatic/bistatic RCS reduction via high-entropy phase-encoded polarization conversion metasurfaces, IEEE Antennas Wirel. Propag. Lett. 18 (6) (2019) 1233–1237.
[76] H. Dai, et al., Ultra-wideband radar cross-section reduction using polarization conversion metasurface, Int. J. RF Microw. Comput. -Aided Eng. 30 (2) (2020) e22085.
[77] C. Fu, et al., Combining Pancharatnam–Berry phase and conformal coding metasurface for dual-band RCS reduction, IEEE Trans. Antennas Propag. 70 (3) (2021) 2352–2357.
[78] M. Long, W. Jiang, S. Gong, Wideband RCS reduction using polarization conversion metasurface and partially reflecting surface, IEEE Antennas Wirel. Propag. Lett. 16 (2017) 2534–2537.
[79] S. Sun, et al., Ultrawideband high-efficiency 2.5-dimensional polarization conversion metasurface and its application in RCS reduction of antenna, IEEE Antennas Wirel. Propag. Lett. 18 (5) (2019) 881–885.
[80] T. Hong, et al., RCS reduction and gain enhancement for the circularly polarized array by polarization conversion metasurface coating, IEEE Antennas Wirel. Propag. Lett. 18 (1) (2018) 167–171.
[81] Y. Liu, et al., Wideband RCS reduction of a slot array antenna using polarization conversion metasurfaces, IEEE Trans. Antennas Propag. 64 (1) (2015) 326–331.
[82] Y. Qi, et al., Ultra-broadband polarization conversion meta-surface and its application in polarization converter and RCS reduction, IEEE Access 8 (2020) 116675–116684.
[83] C. Fu, et al., Dual-band polarization conversion metasurface for RCS reduction, IEEE Trans. Antennas Propag. 69 (5) (2020) 3044–3049.
[84] Z. Zhang, et al., Broadband RCS reduction by a quaternionic metasurface, Materials 14 (11) (2021) 2787.
[85] F. Li, B. You, Complementary multi-band dual polarization conversion metasurface and its RCS reduction application, Electronics 11 (10) (2022) 1645.
[86] J. Chatterjee, A. Mohan, V. Dixit, Ultrawideband RCS reduction of planar and conformal surfaces using ultrathin polarization conversion metasurface, IEEE Access 10 (2022) 36563–36575.
[87] C. Della Giovampaola, N. Engheta, Digital metamaterials, Nat. Mater. 13 (12) (2014) 1115–1121.
[88] T.J. Cui, et al., Coding metamaterials, digital metamaterials and programmable metamaterials, Light.: Sci. Appl. 3 (10) (2014).
[89] X. Yan, et al., Broadband, wide-angle, low-scattering terahertz wave by a flexible 2-bit coding metasurface, Opt. Express 23 (22) (2015) 29128–29137.
[90] L. Liang, et al., Anomalous terahertz reflection and scattering by flexible and conformal coding metamaterials, Adv. Opt. Mater. 3 (10) (2015) 1374–1380.
[91] L.-H. Gao, et al., Broadband diffusion of terahertz waves by multi-bit coding metasurfaces, Light.: Sci. Appl. 4 (9) (2015).
[92] S. Liu, et al., Anisotropic coding metamaterials and their powerful manipulation of differently polarized terahertz waves, Light.: Sci. Appl. 5 (5) (2016).
[93] S. Sui, et al., Fast optimization method of designing a wideband metasurface without using the Pancharatnam–Berry phase, Opt. Express 26 (2) (2018) 1443–1451.
[94] H. Hao, S. Du, T. Zhang, Small-size broadband coding metasurface for RCS reduction based on particle swarm optimization algorithm, Prog. Electromagn. Res. M 81 (2019) 97–105.
[95] H. Gao, et al., An ultra-wideband coding polarizer for beam control and RCS reduction, Front. Phys. 18 (4) (2023) 42301.
[96] F.-f Li, et al., Transmission and radar cross-section reduction by combining binary coding metasurface and frequency selective surface, Opt. Express 26 (26) (2018) 33878–33887.
[97] Y. Saifullah, et al., 4-bit optimized coding metasurface for wideband RCS reduction, IEEE Access 7 (2019) 122378–122386.
[98] H. Dai, et al., An ultra-wide band polarization-independent random coding Metasurface for RCS reduction, Electronics 8 (10) (2019) 1104.
[99] H. Zhang, et al., Coding diffusion metasurface for ultra-wideband RCS reduction, Electron. Lett. 53 (3) (2017) 187–189.
[100] P. Su, et al., An ultra-wideband and polarization-independent metasurface for RCS reduction, Sci. Rep. 6 (1) (2016) 20387.
[101] Y. Saifullah, et al., Multi-bit dielectric coding metasurface for EM wave manipulation and anomalous reflection, Opt. Express 28 (2) (2020) 1139–1149.
[102] L. Ali, et al., Wideband RCS reduction using coding diffusion metasurface, Materials 12 (17) (2019) 2708.
[103] M. Abdullah, S. Koziel, Supervised-learning-based development of multibit RCS-reduced coding metasurfaces, IEEE Trans. Microw. Theory Tech. 70 (1) (2021) 264–274.
[104] X. Liu, et al., A coding diffuse metasurface for RCS reduction, IEEE Antennas Wirel. Propag. Lett. 16 (2016) 724–727.
[105] F. Yuan, et al., Broadband RCS reduction based on spiral-coded metasurface, IEEE Antennas Wirel. Propag. Lett. 16 (2017) 3188–3191.
[106] J.J. Yang, et al., Study of energy scattering relation and RCS reduction characteristic of matrix-type coding metasurface, Appl. Sci. 8 (8) (2018) 1231.
[107] J. Liaori, et al., A new coding metasurface for wideband RCS reduction, Radioengineering 27 (2) (2018) 395.
[108] G. Wu, et al., Ultra-wideband RCS reduction based on non-planar coding diffusive metasurface, Materials 13 (21) (2020) 4773.
[109] F. Yuan, et al., Dual-Mechanism Absorptive Metasurface with Wideband 20 dB RCS Reduction, Crystals 12 (4) (2022) 493.
[110] K. Chen, et al., Coding metasurface for broadband microwave scattering reduction with optical transparency, Opt. Express 25 (5) (2017) 5571–5579.
[111] R. Swain, R.K. Mishra, Phase quantized metasurface supercells for wave manipulation and RCS reduction, Prog. Electromagn. Res. M 74 (2018) 125–135.
[112] X. Li, et al., Suppressing edge back-scattering of electromagnetic waves using coding metasurface purfle, Front. Phys. 8 (2020) 578295.
[113] H.A. Khan, et al., Polarization-Independent Ultra Wideband RCS Reduction Conformal Coding Metasurface Based on Integrated Polarization Conversion-Diffusion-Absorption Mechanism. in Photonics, MDPI, 2023.
[114] Y. Xi, et al., Wideband RCS reduction of microstrip antenna array using coding metasurface with low Q resonators and fast optimization method, IEEE Antennas Wirel. Propag. Lett. 21 (4) (2021) 656–660.
[115] L. Jiu-sheng, L. Shao-he, Y. Jian-quan, Actively tunable terahertz coding metasurfaces, Opt. Commun. 461 (2020) 125186.
[116] J. Song, et al., Broadband and tunable RCS reduction using high-order reflections and salisbury-type absorption mechanisms, Sci. Rep. 9 (1) (2019) 9036.
[117] S. Liu, et al., Full-state controls of terahertz waves using tensor coding metasurfaces, in: ACS applied materials & interfaces, **9**, 2017, pp. 21503–21514.
[118] H. Yang, et al., A programmable metasurface with dynamic polarization, scattering and focusing control, Sci. Rep. 6 (1) (2016) 35692.
[119] Q. Ma, et al., Smart metasurface with self-adaptively reprogrammable functions, Light.: Sci. Appl. 8 (1) (2019) 98.
[120] H.L. Wang, et al., A reconfigurable multifunctional metasurface for full-space control of electromagnetic waves, Adv. Funct. Mater. 31 (25) (2021) 2100275.
[121] J. Zhao, et al., Programmable time-domain digital-coding metasurface for non-linear harmonic manipulation and new wireless communication systems, Natl. Sci. Rev. 6 (2) (2019) 231–238.
[122] A. Shaltout, A. Kildishev, V. Shalaev, Time-varying metasurfaces and Lorentz non-reciprocity, Opt. Mater. Express 5 (11) (2015) 2459–2467.
[123] M. Liu, A.B. Kozyrev, I.V. Shadrivov, Time-varying metasurfaces for broadband spectral camouflage, Phys. Rev. Appl. 12 (5) (2019) 054052.
[124] S.A. Stewart, T.J. Smy, S. Gupta, Finite-difference time-domain modeling of space–time-modulated metasurfaces, IEEE Trans. Antennas Propag. 66 (1) (2017) 281–292.
[125] Z. Liu, Z. Li, K. Aydin, Time-varying metasurfaces based on graphene microribbon arrays, ACS Photonics 3 (11) (2016) 2035–2039.
[126] M.M. Salary, S. Jafar-Zanjani, H. Mosallaei, Time-varying metamaterials based on graphene-wrapped microwires: modeling and potential applications, Phys. Rev. B 97 (11) (2018) 115421.
[127] X. Wang, C. Caloz, Spread-spectrum selective camouflaging based on time-modulated metasurface, IEEE Trans. Antennas Propag. 69 (1) (2020) 286–295.
[128] S.R. Wang, et al., Asynchronous space-time-coding digital metasurface, Adv. Sci. 9 (24) (2022) 2200106.
[129] N. Engheta, Thin absorbing screens using metamaterial surfaces. IEEE Antennas and Propagation Society International Symposium (IEEE Cat. No. 02CH37313), IEEE, 2002.
[130] H. Mosallaei, K. Sarabandi, A one-layer ultra-thin meta-surface absorber. in. 2005 IEEE Antennas and Propagation Society International Symposium, IEEE, 2005.
[131] J. Yang, Z. Shen, A thin and broadband absorber using double-square loops, IEEE Antennas Wirel. Propag. Lett. 6 (2007) 388–391.
[132] M. Li, et al., An ultrathin and broadband radar absorber using resistive FSS, IEEE Antennas Wirel. Propag. Lett. 11 (2012) 748–751.
[133] J.P. Turpin, P.E. Sieber, D.H. Werner, Absorbing FSS ground plane for reduced-Radar Cross Section of conformal antennas. 2013 IEEE Antennas and Propagation Society International Symposium (APSURSI), IEEE, 2013.
[134] Ahmad, H., et al. Microwave absorber using single-layer FSS with wideband operation above the X-band. in 12th European Conference on Antennas and Propagation (EuCAP 2018). 2018. IET.

[135] N.I. Landy, et al., Perfect metamaterial absorber, Phys. Rev. Lett. 100 (20) (2008) 207402.
[136] K.B. Alici, et al., Experimental verification of metamaterial based subwavelength microwave absorbers, J. Appl. Phys. 108 (8) (2010) 083113.
[137] S.D. Assimonis, et al., Absorbing surfaces using EBG structures, IEEE Trans. Magn. 50 (2) (2014) 197–200.
[138] S. Ghosh, et al., An ultrawideband ultrathin metamaterial absorber based on circular split rings, IEEE Antennas Wirel. Propag. Lett. 14 (2015) 1172–1175.
[139] Y. Han, et al., Dual-polarized bandpass and band-notched frequency-selective absorbers under multimode resonance, IEEE Trans. Antennas Propag. 66 (12) (2018) 7449–7454.
[140] S. Ghosh, S. Bhattacharyya, K.V. Srivastava, Design, characterisation and fabrication of a broadband polarisation-insensitive multi-layer circuit analogue absorber, IET Microw., Antennas Propag. 10 (8) (2016) 850–855.
[141] Y. Shen, et al., An extremely wideband and lightweight metamaterial absorber, J. Appl. Phys. 117 (22) (2015) 224503.
[142] S. Ghosh, K.V. Srivastava, An equivalent circuit model of FSS-based metamaterial absorber using coupled line theory, IEEE Antennas Wirel. Propag. Lett. 14 (2014) 511–514.
[143] D. Kundu, A. Mohan, A. Chakrabarty, Design of a conductive fss based ultrathin absorber using impedance analysis method of equivalent circuit model. 2018 IEEE Indian Conference on Antennas and Propogation (InCAP), IEEE, 2018.
[144] M. Hossain, et al., Equivalent circuit design method for wideband nonmagnetic absorbers at low microwave frequencies, IEEE Trans. Antennas Propag. 68 (12) (2020) 8215–8220.
[145] R. Mishra, R. Panwar, D. Singh, Equivalent circuit model for the design of frequency-selective, terahertz-band, graphene-based metamaterial absorbers, IEEE Magn. Lett. 9 (2018) 1–5.
[146] Z. Huang, et al., Tapered resistive sheets and FSS absorber loading for the wide-band RCS reduction of the elliptic surface at TM polarization, IEEE Trans. Antennas Propag. (2023).
[147] Y. Jianing, et al., Compact wideband FSS-absorber-based low-RCS reflectarray antenna, Chin. J. Aeronaut. 36 (6) (2023) 332–339.
[148] P. Tiwari, S.K. Pathak, V. Siju, Design, development and characterization of resistive arm based planar and conformal metasurfaces for RCS reduction, Sci. Rep. 12 (1) (2022) 14992.
[149] D. Kern, D. Werner, Magnetic loading of EBG AMC ground planes and ultrathin absorbers for improved bandwidth performance and reduced size, Microw. Opt. Technol. Lett. 48 (12) (2006) 2468–2471.
[150] T. Deng, Z.-W. Li, Z.N. Chen, Ultrathin broadband absorber using frequency-selective surface and frequency-dispersive magnetic materials, IEEE Trans. Antennas Propag. 65 (11) (2017) 5886–5894.
[151] R. Panwar, et al., Microwave absorption properties of FSS-impacted composites as a broadband microwave absorber, Adv. Compos. Mater. 26 (2) (2017) 99–113.
[152] S. Sui, et al., Absorptive coding metasurface for further radar cross section reduction, J. Phys. D: Appl. Phys. 51 (6) (2018) 065603.
[153] W. Yu, et al., Low-RCS and gain-enhanced antenna using absorptive/transmissive frequency selective structure, IEEE Trans. Antennas Propag. 69 (11) (2021) 7912–7917.
[154] H. Umair, et al., Quarter wavelength Fabry–Perot Cavity antenna with wideband low monostatic radar cross section and off-broadside peak radiation, Appl. Sci. 11 (3) (2021) 1053.
[155] H. Huang, Z. Shen, A.A. Omar, 3-D absorptive frequency selective reflector for antenna radar cross section reduction, IEEE Trans. Antennas Propag. 65 (11) (2017) 5908–5917.
[156] D. Shrekenhamer, W.-C. Chen, W.J. Padilla, Liquid crystal tunable metamaterial absorber, Phys. Rev. Lett. 110 (17) (2013) 177403.
[157] Z. Huang, et al., Tapered resistive sheets loading to the FSS absorber for the wide-angle monostatic RCS reduction applications, IEEE Trans. Antennas Propag. 70 (11) (2022) 11211–11216.
[158] H. Huang, Z. Shen, Low-RCS reflectarray with phase controllable absorptive frequency-selective reflector, IEEE Trans. Antennas Propag. 67 (1) (2018) 190–198.
[159] D. Kundu, et al., Design and analysis of printed lossy capacitive surface-based ultrawideband low-profile absorber, IEEE Trans. Antennas Propag. 67 (5) (2019) 3533–3538.
[160] V.L. Mol, C. Aanandan, An ultrathin microwave metamaterial absorber with enhanced bandwidth and angular stability, J. Phys. Commun. 1 (1) (2017) 015003.
[161] A. Sharma, et al., A miniaturized band-notched absorber for wideband RCS reduction. in 2020. International Symposium on Antennas and Propagation (ISAP), IEEE, 2021.
[162] A. Sharma, S. Ghosh, K.V. Srivastava, A polarization-insensitive band-notched absorber for radar cross section reduction, IEEE Antennas Wirel. Propag. Lett. 20 (2) (2020) 259–263.
[163] Y. Wang, et al., Design of nonresonant metasurfaces for broadband RCS reduction, IEEE Antennas Wirel. Propag. Lett. 20 (3) (2021) 346–350.
[164] S. Koziel, M. Abdullah, Machine-learning-powered EM-based framework for efficient and reliable design of low scattering metasurfaces, IEEE Trans. Microw. Theory Tech. 69 (4) (2021) 2028–2041.
[165] J.P. Wong, A. Epstein, G.V. Eleftheriades, Reflectionless wide-angle refracting metasurfaces, IEEE Antennas Wirel. Propag. Lett. 15 (2015) 1293–1296.
[166] A.A. Fathnan, et al., Characterization of broadband focusing microwave metasurfaces at oblique incidence, IEEE Trans. Antennas Propag. 70 (3) (2021) 2023–2032.
[167] R.L. Haupt, Factors that define the bandwidth of a phased array antenna. 2019 IEEE International Symposium on Phased Array System & Technology (PAST), IEEE, 2019.
[168] J. Shaker, M.R. Chaharmir, J. Ethier, Reflectarray Antennas: Analysis, Design, Fabrication, and Measurement, Artech House, 2013.